Hot Electron Transport and Current Sensing

A thesis presented
by

Mathew Cheeran Abraham

to
The Department of Physics
in partial fulfillment of the requirements
for the degree of
Doctor of Philosophy
in the subject of

Physics

Harvard University
Cambridge, Massachusetts
August 2004

. Author

. **Mathew Cheeran Abraham**

Thesis Co-advisors

Rajeev J. Ram (Massachusetts Institute of Technology)

Robert M. Westervelt (Harvard University)

Hot Electron Transport and Current Sensing

Abstract

The effect of hot electrons on momentum scattering rates in a two-dimensional electron gas is critically examined. It is shown that with hot electrons it is possible to explore the temperature dependence of individual scattering mechanisms not easily probed under equilibrium conditions; both the Bloch-Grüneisen (BG) phonon scattering phenomena and the reduction in impurity scattering are clearly observed. The theoretical calculations are consistent with the results obtained from hot electrons experiments. As a function of bias current, a resistance peak is formed in a 2DEG if the low temperature impurity limited mobilities $\mu_I(T = 0)$ is comparable to $\mu_{ph}(T_{BG})$ the phonon limited mobility at the critical BG temperature. In this case, as the bias current is increased, the electron temperature T_e rises due to Joule heating and the rapid increase in phonon scattering can be detected before the effect of the reduction in impurity scattering sets in. If $\mu_I(T = 0) \ll \mu_{ph}(T_{BG})$, there is no peak in resistance because the impurity scattering dominates sufficiently and its reduction has a much

stronger effect on the total resistance than the rise in phonon scattering.

Furthermore, knowing the momentum relaxation rates allows us to analyze the possible interplay between electron-electron and electron-boundary scattering. The prediction that a Knudsen to Poiseuille (KP) transition similar to that of a classical gas can occur in electron flow [26] is examined for the case of a wire defined in a 2DEG. Concurrently, an appropriate current imaging technique to detect this transition is sought. A rigorous evaluation of magnetic force microscopy (MFM) as a possible candidate to detect Poiseuille electronic flow was conducted, and a method that exploits the mechanical resonance of the MFM cantilever was implemented to significantly improve its current sensitivity.

Contents

Acknowledgments

The work presented in this thesis, and my graduate career as a whole would have been far less meaningful if I had not had the opportunity to work with Professor Rajeev J. Ram. I have been blessed to have had Rajeev's support and understanding on a personal level as well as the awesome experience of standing in front of his "tidal wave" of unbridled enthusiasm for science and engineering over the last six years. If it were not for him, I would have switched careers a long time ago. I thank him for giving me a chance to work in his Physical Optics and Electronics (POE) research group.

There are several members of POE whom I need to thank as I have benefited from their fabulous technical expertise and warm friendships. Margaret Wang was my collaborator for the MFM current sensing project; her work on cantilever dynamics gave me a new appreciation on the wonderful physics that can emerge from studying the simplest of devices. Holger Schmidt, with whom I worked on characterizing nanomagnetic dots, did the theoretical work on nanomagnetic phenomena which gave us great insight into our experimental results. Harry Lee, who has been the backbone of POE, is someone I have relied on several times for his engineering brilliance and incredible eye for detail. Peter Mayer for his analog electronics expertise and general philosophy of "simplicity in design" has been another person whom I have banked on several times. Thomas Liptay, with whom I have had so many great conversations, has taught me both about the economy of words and world economics. Tauhid "Bling" Zaman has reminded me this past year what it is like to be curious and excited about the world. Xiaoyun Guo for her ready smile, home made hot sauce, and useful processing tips. I would also like to mention two past members of the group, Steven

Patterson and Farhan Rana, both of whom contributed to my education in graduate school and inspired me by their discipline to come into lab even on days (and nights) when progress in research seemed almost impossible.

The research presented here was done mainly in the POE group, which is part of the Research Laboratory of Electronics (RLE) at the Massachusetts Institute of Technology (MIT). Some crucial fabrication and measurements were made in shared facilities or through collaborations with other groups at MIT: The 2DEG devices were fabricated in the Microsystems Technology Laboratories (MTL) and in the Nanostructures Laboratory (NSL) of Professor Henry I. Smith. Kurt Broderick of MTL provided crucial advice during the fabrication process. Tim Savas of NSL fabricated the nanomagnetic arrays. All the research was funded by the National Science Foundation (NSF). The MFM measurements were made in a MRSEC sponsored shared facility supported by the NSF at the Center for Material Science and Engineering (CMSE). From outside of MIT, K. Maranowski of Prof. A. Gossard's group at the University of California, Santa Barbara (UCSB) grew the semiconductor hetersotructures out of which the 2DEG devices were made.

As a graduate student at Harvard, I had the good fortune of being taught quantum mechanics by Professor Eric Heller, by far the best course I have taken in physics. My co-advisor Professor Robert Westervelt has been a wonderful source of strategic and real world advice; it was great to have him as a resource. Also, my yearly meeting with Professor Michael Tinkham was one I always look forward to; his frank opinion on any topic under the sun and sage advice on career matters is appreciated.

On a more personal note, the years I have spent in graduate school have been

truly transforming, and there is the urge to name all that have supported me in one way or the other through these wonderful years. Unfortunately this would be a list that would be extraordinarily long and make my brief thesis look even shorter. I have to mention though my immediate family. My parents for their unconditional love and support from so far away, my brother Mon and sister-in-law Rahel for their constant encouragement and help in keeping things in perspective, Jyotsna and Dhiraj for always being there to share good times and challenging ones, and of course my beloved wife Danielle for being a constant source of spiritual and intellectual nourishment. Danielle's companionship and love has been a source of immense happiness to me, and it is with great excitement that I look forward to our life together which promises to be full of many wonderful experiments.

This thesis is dedicated to my teachers. As my formal education comes to an end, I cannot help but recall all of those who have taught me. It is through their generosity that I have learnt all that I know. I thank them for their gift of knowledge and wisdom.

. Mathew Cheeran Abraham

. Cambridge, MA August, 2004

Dedicated to my teachers.

Chapter 1

Introduction

1.1 Motivation

Mesoscopic solid-state electronic devices have been the subject of study for more than a quarter century [22] [3]. In these devices, electron transport is ballistic, i.e. electron momentum scattering lengths are much greater than the device dimensions. Scientists have been able to explore this regime because of the remarkable advances in lithographic and semiconductor crystal growth technologies. Arguably, the sights of scientists have shifted rapidly from macro-scale to nano-scale structures, exploiting and contributing to ever smaller fabrication and materials technologies. This dissertation has been inspired by a careful (and in some sense retrospective) examination of various important length scales that are relevant to electron transport.

The transport properties of high-mobility AlGaAs/GaAs heterostructure quantum well confined two-dimensional electron gases (2DEGs)[1] have been studied extensively [3], and is the material system that we focus on. This system has for many years served as the ideal "play ground" to study electron dynamics because the host crystal can be grown with almost atomic precision, the channel where the electrons flow has very few impurities, and at low temperatures it has a simple spherical Fermi surface [22]. In order to advance our understanding of the temperature dependence of the various scattering processes in a 2DEG, we explore transport of "hot" electrons, i.e. electrons that have a temperature T_e higher than the lattice temperature T_L. It is found that using hot electrons, it is possible to probe the Bloch-Grüneisen (BG) phenomena which is extremely difficult to observe under equilibrium conditions in semiconductors when $T_e = T_L$. Also, by analogy to classical gases, we specify the

[1] In this thesis the acronym "2DEG" will be used to refer to only high-mobility AlGaAs/GaAs heterostructure 2DEG systems.

conditions under which it should be possible for viscous effects in 2DEGs to arise from increased electron-electron scattering.

The electron-electron scattering length l_{ee} sets the length scale for classical viscous fluid-like structure in the electron velocity profiles. Non-perturbative current imaging at the l_{ee} scale is the most comprehensive way to determine if viscous effects influence the velocity of electrons inside a device. In the hope of eventually "imaging" viscous electron flow structure, a concerted effort into understanding the resolution limits of magnetic force microscopy (MFM) was conducted. MFM was chosen because it is the magnetic imaging technique with the best spatial resolution [9]. However, it has the drawback of being the least magnetically sensitive [9]. To increase the sensitivity of MFM to sense currents, a novel mode of operation was implemented. In the next two sections, we provide background information that offers further context into the research described in the subsequent chapters, and we end this chapter with an outline of the structure of this thesis.

1.2 Introduction to 2DEGs

1.2.1 AlGaAs/GaAs heterostructure

The schematic of a GaAs/$Al_{0.3}Ga_{0.7}As$ heterostructure grown by molecular beam epitaxy (MBE)[2] shown in Fig.1.1(a) is the crystal used to conduct our experiments. At low temperature, an electron gas is formed at the location indicated and is referred to as a two-dimensional electron gas (2DEG).

[2]The heterostructure was grown by Kevin Maranowski in the group of Arthur Gossard at the University of California, Santa Barbara.

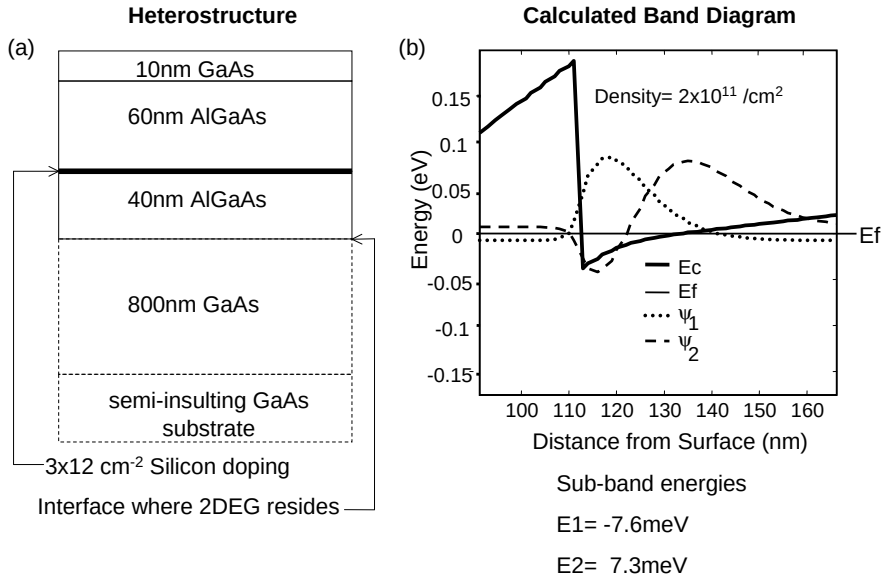

Figure 1.1: (a) Schematic diagram (not to scale) of structure of crystal grown using (MBE) (b) Plot of conduction band E_c at the AlGaAs/GaAs interface where the 2DEG resides at T =2K. Also shown are, the first two sub-band wavefunctions ψ_1 and ψ_2. The corresponding eigen-energies are calculated w.r.t. the Fermi level which is set to 0eV. Also indicated is the estimated electron density of the 2DEG.

The numerical one dimensional calculation of the conduction band is shown in Fig.1.1(b) [3]. The calculations used a finite difference technique to solve the one dimensional Poisson and Schrödinger equations in a self-consistent manner. The shape of the quantum well (QW) that confines the motion of the electrons in a single plane is approximately triangular. The subband energy levels are at -7.6 meV and 7.3 meV for the first and second energy levels respectively, relative to the Fermi energy $E_f \equiv 0$ meV. Fig. 1.2 shows that as the electron gas temperature is reduced, n_2/n_1

[3]Band structure calculations were made using a software program developed by Professor G.L. Snyder, University of Notre Dame

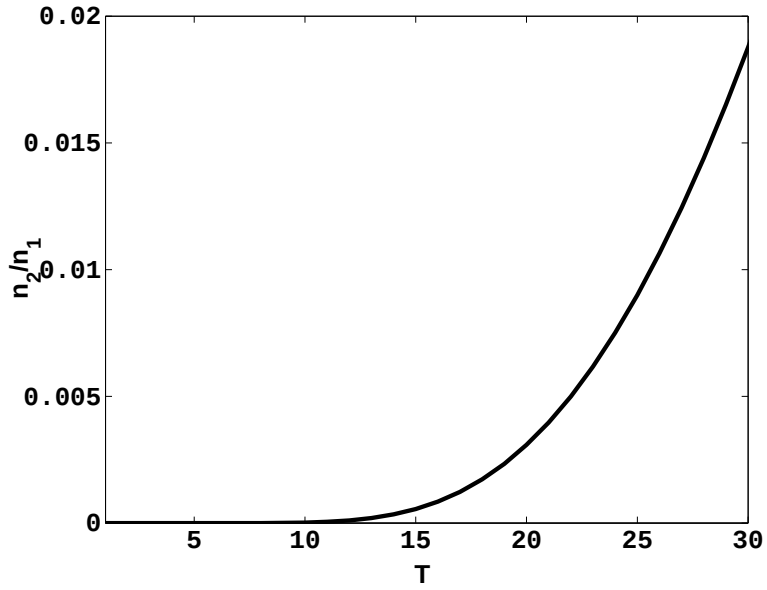

Figure 1.2: The ratio of the second to first subband electron density n_2/n_1 is plotted as a function of temperature T. The electrons are >99.5% in the first subband for T=20 K and >98% at T=30 K.

becomes smaller thus further strengthening its 2D nature. The ratio of the first to the second subband populations n_2/n_1 is <0.005 at 20 K and <0.02 at 30 K.

At low temperatures, the Schottky barrier between lithographically fabricated metal electrodes and the semiconductor surface prevents current from flowing when a negative voltage is applied to the gate. The electric field created by this "Schottky gate" reduces the density of electrons in the 2DEG below it. A sufficiently large negative voltage depletes the electron gas, forming an insulating region under the gate. In order to form "Ohmic" contacts with the 2DEG, an alloy of Au and Ge needs to be deposited on the surface of the heterostructure and annealed rapidly, thereby causing the alloy to diffuse into the quantum well. Details of the exact fabrication steps performed to realize our device are presented in Appendix A. Schottky gates

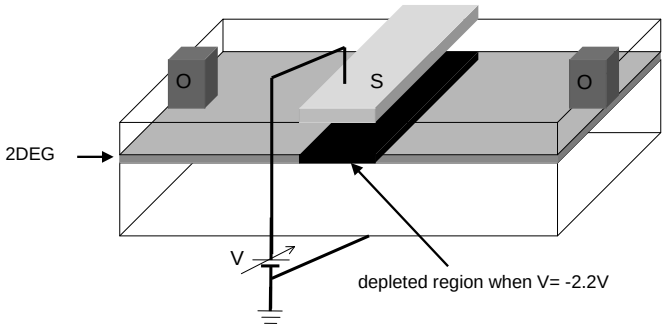

Figure 1.3: A schematic diagram (not to scale) of two ohmic contacts connected to the 2DEG labeled 'O' and a Schottky gate labeled 'S'. When a negative bias of -2.2V is applied to S, the electron gas beneath it is completely depleted and the conductance between the ohmic contacts drops to zero.

are a convenient way of defining the geometry of extremely small devices. Fig. 1.3 shows a schematic diagram of the experiment that was conducted to determine the electrostatic potential needed to be applied to a Schottky gate in order to deplete the electron gas below it. It was found that a voltage of -2.2 V on the gate electrode marked 'S' was sufficient to stop the conduction of electrons between the two ohmic contacts marked 'O'.

1.2.2 Basic 2DEG transport phenomena

AlGaAs and GaAs have a lattice mismatch of only a few percent and therefore the strain is minimal at the interface making it close to defect-free. In addition, the ionized donor impurities are spatially separated from the channel which dramatically

reduces the impurity scattering of electrons as compared to bulk semiconductors of similar electron densities. The resulting high electron mobilities of typical 2DEGs are $\mu \approx 10^6 \mathrm{cm}^2/\mathrm{Vs}$, corresponding to an extremely long momentum relaxation length of $l_m = v_F < \tau_m > \approx 10\mu\mathrm{m}$, where v_F is the Fermi velocity for an electron density $n=2\times10^{11}/\mathrm{cm}^2$ and $< \tau_m >$ is the momentum scattering time. The mobility of a material μ is defined as the ratio of the drift velocity v_d to the applied electric field $\mathcal{E}$ and it can be shown that,

$$\mu = \left|\frac{v_d}{\mathcal{E}}\right| = \frac{e < \tau_m >}{m} \tag{1.1}$$

where, e is the magnitude of the electric charge, m is the effective mass of the electron and $< \tau_m >$ is the effective momentum relaxation time. There could be several momentum scattering processes that contribute to $< \tau_m >$. For a given scattering process S^i if we calculate the momentum relaxation time $< \tau_m^i >$ then by Matthiessens's rule,

$$\frac{1}{< \tau_m >} = \sum_i \frac{1}{< \tau_m^i >}. \tag{1.2}$$

From 1.1 and 1.2, one can infer that if any one momentum scattering time $< \tau_m^j >$ is significantly smaller than all the other momentum scattering times $< \tau_m^{i\neq j} >$, then $\mu \approx \frac{e<\tau_m^j>}{m}$. Consequently, even the temperature dependence of μ follows the temperature dependence of $< \tau_m^j >$ and the temperature dependence of all the other less dominant momentum scattering times $< \tau_m^{i\neq j} >$ remain "hidden".

From Figure1.4, taken from Pfeiffer *et al.* [51], a historical perspective on the evolution of 2DEG technology is gained. In older 2DEGs, the mobility is dominated by impurity scattering up to $T \approx 100$ K. The superior mobilities of modern 2DEGs are brought about in large part by improving the spatial separation of the donor

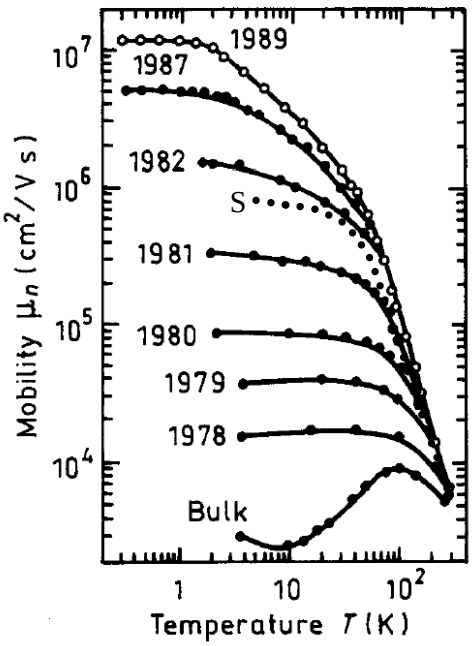

Figure 1.4: This graph taken from Pfeiffer *et al.* [51] shows the evolution of AlGaAs/GaAs 2DEG technology. All the samples are limited by impurity scattering at low temperatures. As the technologies of modulation doping and delta doping allowed the impurities to be placed further away from the transport channel, mobilities improved. The fall in μ in the highest mobility samples is caused by the increase in phonon scattering. In the temperature range 5-50K, acoustic phonon scattering dominates, above which optical phonon scattering and inter-subband scattering take over. For the old 2DEG samples the mobility initially improves slightly as a function of temperature. The dotted curve labels 'S' is the mobility curve of the sample in Figure 1.1. This sample has a moderately high mobility of 0.82×10^6 cm^2/Vs.

impurities from the conduction channel. This has been done by techniques such as introducing an undoped "spacer" layer, modulation doping, and delta doping. Modern 2DEGs can have mobilities in the 10^6-10^7 cm^2/Vs range. The mobility curve overlayed on this graph labeled 'S', corresponds to that of the 2DEG sample with which our experiments are conducted (crystal structure provided in Figure 1.1). In modern samples, the mobility is limited by impurity scattering below $T \approx 6$K, by

acoustic phonon scattering in the 6-60 K range and by optical phonon and intersubband scattering for temperatures above ≈60K [19].

The temperature range from 6-60K, where acoustic phonon scattering dominates, has a T^{-1} temperature dependence. The inverse temperature dependence occurs because the acoustic phonon scattering process is proportional to the phonon population $N \approx k_B T$ at these temperatures. This temperature range is referred to as the equipartition regime. As the temperature is lowered even further, the phonon dependent scattering process falls off precipitously and switches to a T^{-5} dependence below a critical temperature $T_{BG} \approx 2\hbar s k_F$ where k_F is the Fermi wavenumber, $\hbar$ the Plank constant, s the speed of sound, and k_B the Boltzmann constant [56]. For typical 2DEG densities of 2×10^{11}cm^2/Vs, the transition temperature $T_{BG} \approx 6$K. Coincidentally, even for the highest mobility samples, impurity scattering dominates below T_{BG} and therefore the T^{-5} dependence of the phonon scattering is not easy to detect [68]. This transition occurs because of phase space restrictions arising out of the Pauli exclusion principle that prevent degenerate electrons from emitting phonons with enough momentum to cause large angle scattering. This phenomena is called the Bloch-Grüneisen (BG) transition because a similar transition occurs in pure metals [85] [4]. A quantitative account of the BG phenomena will be discussed in greater detail in Chapter 2.

The impurity scattering dominates at the lowest temperatures, preventing the easy observation of the T^{-5} dependence of the phonon momentum scattering process. And, the temperature dependence of the impurity scattering is "hidden" as

[4] In pure metals, for $T \ll \Theta_D$ the Debye temperature, phonon scattering has a T^{-5} dependence and for $T \gg \Theta_D$ is linear in T. This transition occurs because it is not until $T > \Theta_D$ that all the phono modes are excited in a metal [85].

the phonon scattering dominates in the T=6-60 K range where the impurity scattering actually reduces. Using the Sommerfeld approximation, it can be shown that impurity dependent mobility is given by,

$$\mu_I(T) = \mu(0)\left(1 + \frac{\pi^2}{6}\gamma(\gamma+1)\left(\frac{k_B T}{E_F}\right)^2\right), \tag{1.3}$$

where, $\gamma \approx 1.5$ [30]. This actual increase in mobility is only observed in older 2DEG samples where impurity scattering remains more dominant than phonon scattering for a much larger temperature range.

In Chapter 2 we present theoretical calculations and experimental results for both equilibrium measurements of mobility where the electron temperature $T_e = T_L$ the lattice temperature and for "hot" electrons where $T_e > T_L$. We find that in the case of hot electrons, the mobility can be a non-monotonic function of T_e. The actual shape of the mobility curve for hot electrons can only be explained by taking into account the B-G effect and the reduction in impurity scattering, as discussed above.

1.2.3 Electron-electron scattering

Normally one assumes electron-electron (e-e) scattering does not contribute to the classical resistance of an electronic device. This is because, with the exception of Umklapp scattering, e-e scattering conserves momentum. Also, the diffusion of electron momentum perpendicular to the direction of current occurs more efficiently for most electronic materials through scattering processes other than e-e scattering. In a 2DEG, mobilities are large enough that it is possible to tune the e-e scattering l_{ee} to be either greater or smaller than the transport length l_m by adjusting the electron temperature T_e and keeping the lattice temperature T_L pinned at a low value [13][20].

If l_{ee} can contribute sufficiently to momentum diffusion, then it is conceivable that viscous effects similar to classical gases could occur. In a classical gas it can be shown that the viscosity η_c is given by,

$$\eta_c = \frac{1}{2}\bar{m}n\bar{v}l, \tag{1.4}$$

where $\bar{m}$ is the mass of the particles of the gas, n the density, $\bar{v}$ the thermal velocity and l the mean free path [43]. For a Fermi gas, the analogous expression for viscosity is $\eta_F \sim \bar{m}nv_Fl$ [43], and therefore we could expect the viscosity of a 2DEG to be

$$\eta_e \sim mnv_Fl_{ee} \tag{1.5}$$

where, m is the effective mass of the electron.

For a gas, the Knudsen number K_n is the ratio W/l where W is the characteristic length scale of the device in which the gas in contained. In systems with $K_n < l$, gases behave like continuous media, and fluid dynamic equations such as the Navier-Stokes equation apply [17]. The transition from large K_n to small K_n in CO_2 gas was first studied by Knudsen in 1909 [37]. The same transition has been investigated in normal ^{3}He system by Parpia and Rhodes [50]. In both the case of classical gas CO_2 and Fermi gas ^{3}He, a minimum was measured in the conductance of the system as a function of K_n, which is referred to as the Knudsen minimum. In 1963, Gurzhi [26] predicted a conductance minimum in impurity free conductors. Experiments have been conducted to observe this effect in metal wires [83] and 2DEGs [20]. However, alternative possible explanations (Zhao *et al.* [84] in the case of metals and Gurzhi *et al.*[27] in the case of 2DEGs) have have been put forward to explain the experimentally observed minimum in conductance.

In the transition from large K_n to small K_n, viscosity sets in and affects the velocity profile of moving fluids. In the case of fluid flowing through a pipe, the velocity profile is relatively flat for large K_n and becomes parabolic with a curvature proportional to the viscosity (Poiseuille flow) as Kn increases [18]. A similar switch in the drift velocity profile of electrons in electrical wires is predicted [26]. In the last section of Chapter 2, we specify conditions under which the Knudsen to Poiseuille (K-P) transition could occur in 2DEGS. In order to unambiguously detect the the K-P transition, we need to be able to "image" the velocity profile of currents. From Ampere's Law, a moving charge in a device produces a magnetic field. Therefore, we pursued determining the limits of magnetic force microscopy (MFM) as a microscopic magnetic sensing technique which could possibly "image" viscous fluid-like phenomena in electron flow.

1.3 Microscopic magnetic imaging

1.3.1 Survey of non-destructive magnetic imaging techniques

Over the last decade, MFM has become a powerful tool for the magnetic recording head industry, which continually strives to develop higher density magnetic storage media [53]. The integrated circuit (IC) industry similarly demands smaller circuits for higher transistor density on a chip, which lowers costs and enables greater portability. However, non-destructive current sensing at microscopic length scales remains a challenge that has yet to be surmounted. Such a technique would provide valuable information for quality assurance and failure detection.

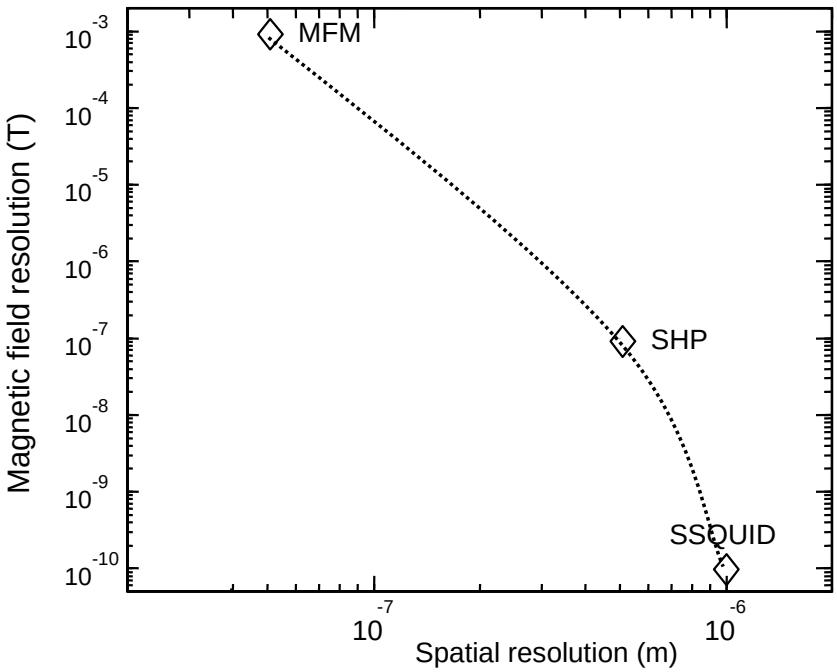

Figure 1.5: The magnetic sensitivity of the best spatial resolution achieved to date by MFM [14], SHM [62] and SSQUID [74] are marked. Most combinations of spatial resolution and magnetic sensitivity to the right of the dotted line joining these points can be attained using either one or more of these magnetic microscopies.

As mentioned earlier, Ampere's Law tells us that a moving charge in a device produces a magnetic field. Therefore, by scanning a suitable magnetic sensor over the current carrying device, images of current flow can be constructed. Several magnetic imaging techniques are available and have also been used to image current. However, a tradeoff between spatial resolution and magnetic field sensitivity separates the different methods to specific applications and needs. In Figure 1.5, the best spatial resolution performance of MFM, scanning hall probe (SHP), and scanning superconducting quantum interference device (SSQUID) microscopies reported

to date is marked. The dotted line connects these points and approximately divides the graph into regions of combined spatial resolution and magnetic sensitivity that has been attained (to the right of the line) from that which is yet to be attained (left of the line). Among the leading non-destructive techniques, scanning superconducting quantum interference device (SSQUID) microscopy [76] offers the best magnetic field sensitivity of approximately 100pT [9]. The two main disadvantages of SSQUID microscopy are that its spatial resolution is limited to ≈ 1 μm because of lithography technology constraints and that it requires sensor operation at low temperatures [74] [36]. Scanning Hall probe microscopy (SHP) consists of a Hall bar integrated onto a scanning probe [15]. It measures the Hall resistance of the bar in the presence of magnetic field, which is directly proportional to the magnetic field through the bar itself. The spatial resolution of SHP depends on the proximity of the Hall probe to the sample and the size of the hall bar. The magnetic field resolution of SHP is about 100nT [9], and the spatial resolution of the hall probe has been demonstrated to be $<0.5\mu$m [62]. Since our objective is to "image" viscous electron flow, the spatial resolution we need is significantly less than the e-e scattering length l_{ee} $\approx$400nm, which is the source of viscosity (in Chapter 2, we further explore the origins of this length scale). The only magnetic microscopy with spatial resolution significantly less than 1μm is MFM.

1.3.2 Introduction to MFM

MFM involves scanning a magnetically coated sharp tip over a sample that is emanating a magnetic field. In Figure 1.6, a schematic of a typical MFM is shown.

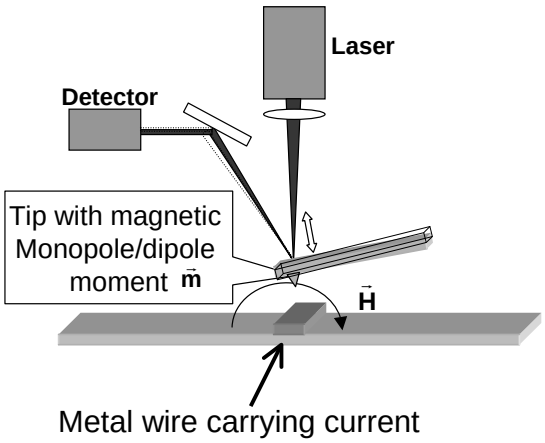

Figure 1.6: MFM can be used to sense currents as the magnetic tip experiences a force because of the presence of a magnetic field **H** produced by any current carrying device.

The magnetic tip, which is attached to a cantilever, experiences a force in the presence of a magnetic field which causes a displacement of the cantilever. This displacement can be detected by measuring the deflection of a laser beam that reflects off the back of the cantilever.

Of all the scanning magnetic sensor microscopies that have been developed, Magnetic Force Microscopy (MFM) has the highest spatial resolution [9]. MFM has been used to detect magnetic field gradients down to sub-50 nm length scales [14][52][66]. However, the magnetic sensitivity it provides is only in the 1 mT range, which is significantly less than what is possible with SHP and SSQUID techniques [9]. As a result, MFM has been used to measure currents only down to $\approx$ 1 mA [38]. This low current sensitivity limits the application of MFM current sensing to the study of phenomena like electromigration [80] and current crowding [81], where currents

are relatively high. Viscous effects in micron-sized wires could occur in a 2DEG for currents in the microampere range as discussed in Chapter 2. If MFM could measure currents significantly below the microampere range, then not just electron viscosity but also important failure mechanisms in IC circuits, such as cross talk [79] and current leakage [34], could possibly be studied with unprecedented spatial resolution.

In Chapter 3, it is shown that if MFM is used to sense AC instead of DC currents, two orders of magnitude in current sensitivity can be gained. Further, the two methods are qualitatively different in that the DC method measures the gradient of the magnetic field and the AC method measures the magnetic field itself (under the monopole approximation). However, the gain in current sensitivity is offset by an apparent dramatic loss in spatial resolution. The theoretical models used to describe cantilever and magnetic tip-sample interaction are presented, and then compared to experimental results obtained from AC and DC current sensing using MFM.

1.4 Structure of this thesis

The main body of this thesis falls naturally into two parts which are relatively independent but coupled through the guiding motivation of understanding electron transport as stated above.

The two parts are:

- Hot electron transport in 2DEGs. (Chapter 2)
- Microscopic current sensing using MFM. (Chapter 3)

The thesis ends with Chapter 4 which summarizes conclusions and important fu-

ture work that could be undertaken as a natural extension of the presented results. For completeness, an Appendix is included which contains details regarding: Fabrication of 2DEG devices and cryogenic electrical measurements - Appendix A, and theoretical calculations - Appendix B.

Chapter 2

Hot Electron Dynamics in a 2DEG

2.1 Introduction

The transport properties of high mobility 2DEGs have been extensively studied in the last few decades [3] [7] [69]. Most experiments and theory have focused on either quantum or many-body effects at low temperature, or at higher temperatures for electronics where optical phonon scattering and intersubband scattering dominate. We present theoretical calculations and experimental results in the regime of "hot" electrons where the electronic temperature is greater than the lattice temperature $T_e > T_L$ but both T_e and T_L are low enough that intersubband and optical phonon scattering are unimportant[1]. In this regime the temperature dependence of the impurity and acoustic phonon momentum scattering processes emerge clearly.

An illustration of transport regimes that are easily observed in hot electron 2DEGs is the Bloch-Grüneisen (BG) phenomena. As mentioned in Chapter 1, the BG phenomena refers to phase space restrictions which occur at low temperatures that prevent electrons from emitting phonons with sufficient momentum so as to cause large angle scattering. The critical temperature at which this effect occurs is given by $T_{BG} \approx 2k_f\hbar s/k_B$, where s is either the longitudinal or transverse speed of sound in the crystal depending on the which phonon branch is being considered, and k_F is the Fermi wave vector. In equilibrium (where $T = T_e = T_L$), the phonon limited mobility μ_{ph} for temperatures below T_{BG}, has a T^{-5} dependence as compared to T^{-1} for temperatures above T_{BG}. Since the mobility of 2DEGs are generally dominated by impurity scattering (coincidentally) at temperatures up to and above T_{BG}, the temperature dependence of acoustic phonon scattering that is the hallmark of BG

[1]This regime is sometimes referred to in the literature as "warm" electrons [82].

phenomena can be extremely difficult to observe.

The BG effect on momentum scattering was extracted from equilibrium mobility measurements by Stromer *et al* [68], see Figure 2.1(a). In their experiment, the temperature dependence of μ_{ph} was extracted from the equilibrium mobility data of an ultra-high mobility 2DEG. This was done by deducting progressively larger estimated values of impurity limited mobility μ_I (which was assumed to be roughly constant at and below T_{BG}) from the total mobility data measured. By subtracting a constant value of μ_I=11.6$\times$10^{6}cm^2/Vs, the temperature dependence of the remaining mobility component matched the theoretically calculated μ_{ph}, thus revealing the BG transition. This experiment required an extremely high mobility sample and very precise electronics to reveal the BG phenomena.

If in the future 2DEGs are produced with $\mu_I(0)$ significantly larger than $\mu_{ph}(T_{BG})$, the BG effect would be detected relatively easily in an equilibrium measurement of mobility. However, for most 2DEGs available today, $\mu_I(0)$ is much larger than $\mu_{ph}(T_{BG})$, and the initial fall in equilibrium mobility μ as a function of T until $T = T_{BG}$, where phonon scattering is in the BG regime, is not easily distinguished from the equipartition regime where the mobility falls as a result of an increase in the phonon occupancy. In Figure 2.1(b) are plotted the various mobility components calculated using the theory presented in detail in the following section. The BG transition occurs at T_{BGL} =5.3K for the deformation coupled acoustic phonon scattering and piezoelectric longitudinal mode coupled acoustic phonon scattering, and T_{BGT} =9.1K for the piezoelectric transverse mode coupled acoustic phonon scattering.

In this Chapter we discuss theoretical calculations and experimental data which

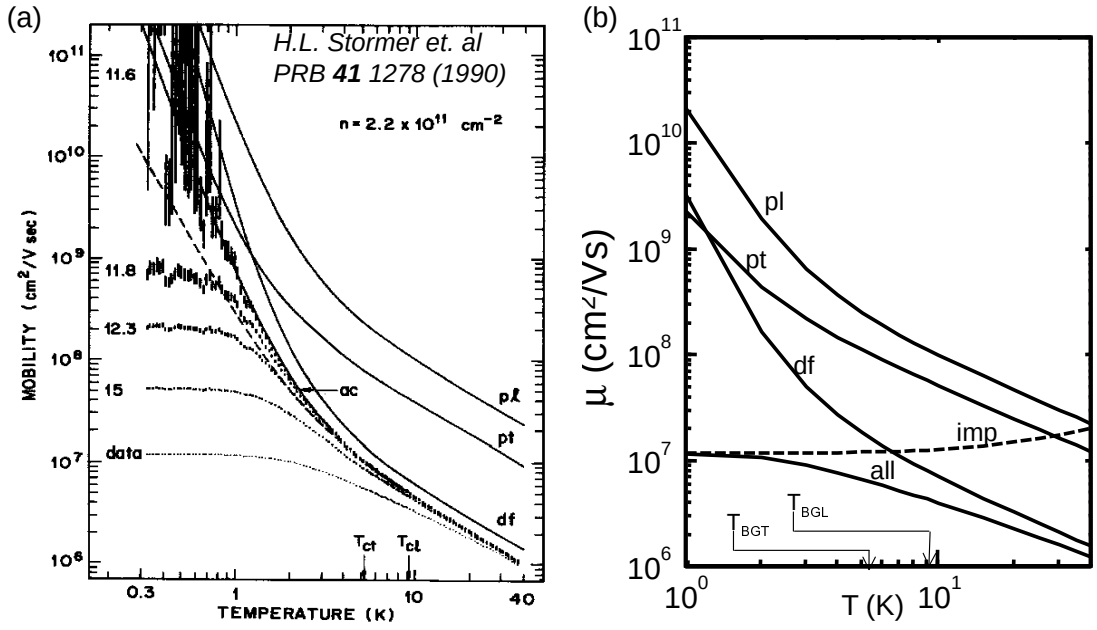

Figure 2.1: The experimental results of Stromer *et al.* [68] are shown in (a). The temperature dependence of the phonon scattering limited mobility μ_{ph} was extracted from the equilibrium mobility data of an ultra-high mobility 2DEG. This was done by deducting progressively larger estimated values of impurity limited mobility μ_I (which was assumed to be roughly constant at and below T_{BG}) from the total mobility data measured. By subtracting a constant value of μ_I=11.6$\times 10^6$cm^2/Vs, the temperature dependence of the remaining component matched the theoretically calculated μ_{ph}, thus revealing the BG transition. In (b) is plotted the results of the calculations using the theoretical model detailed in this Chapter, assuming the same specifications of density n and zero temperature mobility $\mu_I(0)$ as that of (a). The labels *pl* and *pt* stand for the piezoelectrically coupled acoustic phonon scattering for the longitudinal and transverse modes respectively, *dp* the deformation coupled acoustic phonon scattering, *imp* the impurity scattering, and *all* the combined mobility including all the components together.

show that for 2DEGs with low temperature mobilities of 2.2$\times$ 10^{6}cm^2/Vs, the mobility as a function of T_e, with T_L fixed at 1.5K, falls till $T_e \approx T_{BG}$, and then rises. It is demonstrated that the initial drop in the mobility as T_e increases occurs as a result of the BG effect, and the rise in mobility is caused by a reduction in impurity scattering.

This simple result demonstrates that the BG effect can be detected relatively easily using hot electrons. In addition, by pinning T_L to 1.5K, the phonon scattering due to phonon absorption is restricted and therefore the temperature dependence of the impurity scattering is observed.

In the sections to follow, we first present the electron temperature model (ETM) of hot electrons in a 2DEG, which was first proposed by Price [56] [55]. The ETM is then applied to explain our experimental results. The Chapter ends with a discussion on the possibility of viscous effects occurring in hot electrons flowing through a 2DEG wire with rough boundaries.

2.2 Theoretical model

The ETM model makes several assumptions. The most basic assumption is that the electron gas subject to an applied electric field is not perturbed significantly from the finite temperature Fermi distribution f and therefore an electron temperature T_e can be defined [55]. Also implicit in the ETM is the assumption that the drift velocity v_d is small compared to the sound velocity s and Fermi velocity v_f and therefore non-equilibrium phonon effects and dynamical screening is not incorporated. At high fields, if $v_d \gtrsim s$ and the electron distribution is perturbed significantly from f, then the ETM fails and considerably underestimates the phonon scattering rate [40][41].

In the ETM, the momentum scattering is calculated under the relaxation time approximation (RTA). RTA assumes that there is a characteristic time scale $< \tau_m >$ in which the perturbed distribution would relax to the Fermi distribution and that the perturbation can be approximated by $E\frac{\partial f}{\partial E}$. Also, Matthiesen's rule (Equation

1.1), is applied in combining the effects of the momentum and energy relaxation processes. Matthiesen's rule applies when the scattering processes occur independent of each other and when the energy dependence of the various scattering processes are similar [5]. Even though the energy dependence of impurity scattering and phonon scattering differ, Price argues in Reference [55] that the Matthiessen's rule is still a good approximation for degenerate electron gas distributions.

We apply the ETM in the following manner. As a function of Te and T_L (with $T_e \geq T_L$), the mobility μ and the net power loss P_e for a 2DEG are calculated separately. Subsequently, it is possible to map μ to a given P_e, for a fixed T_L. For a 2DEG, P_e is very small when both T_L and T_e are below 30K (see Figure 2.4). Hence, when power is supplied to the 2DEG, at a fixed T_L, through an externally applied electric field, T_e and P_e rise till there is no net energy gain to the 2DEG. Ideally, in our experiments both T_L and T_e should be measured, enabling a more direct comparison of experimental and theoretical estimates of μ. Since only T_L and input power is known, we need to resort to the energy relaxation calculations to compare experimental data with our theoretical calculations.

2.2.1 Momentum relaxation

The momentum relaxation processes have been calculated in detail in references [35] [77] [56] [30]. For completeness, we restate these theoretical results with the notation used in reference [30]. The basic equations are presented in this chapter and the details are in Appendix B. As stated in Chapter 1, the mobility of a material $\mu = \frac{e<\tau_m>}{m}$, where $< \tau_m >$ is the total momentum relaxation time arising from the

reciprocal summation of the individual scattering times $< \tau_m^i >$ given by $\frac{1}{<\tau_m>} = \sum_i \frac{1}{<\tau_m^i>}$. The notation $< . >$ implies an ensemble average, which in the relaxation time approximation is given by [45],

$$\frac{1}{< \tau_m^i >} = \frac{\int_0^\infty \frac{1}{\tau_m^i(E)} E \frac{\partial f}{\partial E} dE}{\int_0^\infty E \frac{\partial f}{\partial E} dE} \tag{2.1}$$

where,

$$f = \frac{1}{e^{\frac{E-E_F}{k_B T_e}} + 1} \tag{2.2}$$

is the equilibrium Fermi distribution with Fermi energy E_F and electron temperature T_e. In our calculations we consider the two most dominant scattering processes, impurity scattering and phonon scattering.

Impurity scattering

Impurity scattering is elastic, therefore the initial and final in-plane wave vector electronic states $\mathbf{k_1}$ and $\mathbf{k_2}$ of an electron have the same magnitude $k = |\mathbf{k_1}| = |\mathbf{k_2}|$. The scattering rate as a function of electronic kinetic energy $E = \hbar^2 k^2 / 2m$ is given by

$$\frac{1}{\tau_m^I(E)} = \frac{m}{\hbar^3} \frac{4}{(2\pi)^2} \int_0^\pi d\theta (1 - \cos\theta) \int_0^\infty dz_I N(z_I) \frac{|F(q_{xy}, z_I)|^2}{q_{xy}^2 \epsilon^2(q_{xy}, T_e)} \tag{2.3}$$

where, m is the effective mass of the electron in GaAs, $N(z_I)$ is the impurity distribution function, $F(q_{xy}, z_I)$ is a form factor that is the Laplace transform of the square of the first quantized wavefunction taken relative to the impurity location (detailed expression found in Appendix B), $\epsilon(q_{xy}, T_e)$ is the static wave vector and temperature dependent screening function as calculated by Stern [67], θ the scattering angle between $\mathbf{k_1}$ and $\mathbf{k_2}$, and the magnitude of the scattering wave vector

$q_{xy} = |\mathbf{k_2} - \mathbf{k_1}| = 2k\,|\sin(\theta/2)|$. The impurity scattering time $\tau_m(E) \propto E^{1.5}$ [30], which implies that as T_e rises impurity scattering reduces because the electrons become more energetic. The impurity related mobility $\mu_I(T) \approx \mu_I(0)(1 + O(T/T_F)^2)$, where $\mu_I(0)$ is the impurity related mobility at $T_e = 0$ and $T_F = E_F/k_B$ is the Fermi temperature.

Phonon scattering

The energy dependent scattering rate for acoustic phonon scattering is given by

$$\frac{1}{\tau_m^p(E)} = \frac{m}{\hbar^3}\frac{4}{(2\pi)^2}\int_0^\pi d\theta(1-\cos\theta)\int_0^\infty dq_z\,|I(q_z)|^2\,\frac{|C^p(q)|^2}{\epsilon^2(q_{xy},T_e)} \times G(E,\hbar\omega_q) \qquad (2.4)$$

where, $|C^p(q)|^2$ is the scattering matrix element, $|I(q_z)|^2$ is the Fourier transform of the first quantized wave function. The energy of the acoustic phonon $\hbar\omega_q = \hbar sq$ with $q = \sqrt{q_{xy}^2 + q_z^2}$ being the wave vector. The term $G(E,\hbar\omega_q)$ given by

$$G(E,\hbar\omega_q) = \frac{1}{1-f(E)}\{N_q(1-f(E+\hbar\omega_q)) + (N_q+1)(1-f(E-\hbar\omega_q))\} \qquad (2.5)$$

keeps track of the phonon and electron population statistics with,

$$N_q(\varepsilon) = \frac{1}{(e^{\frac{\hbar\omega_q}{k_B T_L}} - 1)} \qquad (2.6)$$

being the Planck distribution which is the equilibrium phonon occupation number for a given lattice temperature T_L. The interesting temperature dependence with respect to phonon scattering is contained in the $G(E,\hbar\omega_q)$ term. As the temperature is lowered, N_q tends to vanish so the term associated with momentum absorbtion goes to zero. Further more, as illustrated in Figure 2.2, the phase space constraints cause the BG effect. At temperatures below T_{BG}, electrons participating in transport

are only just above the Fermi surface and are not able to emit phonons that can significantly change their momentum because all the underlying states are filled. At temperatures above T_{BG}, the phase space restrictions ease, and $N_q \approx k_B T_L/\hbar\omega_q$ therefore the scattering rate becomes linear with temperature.

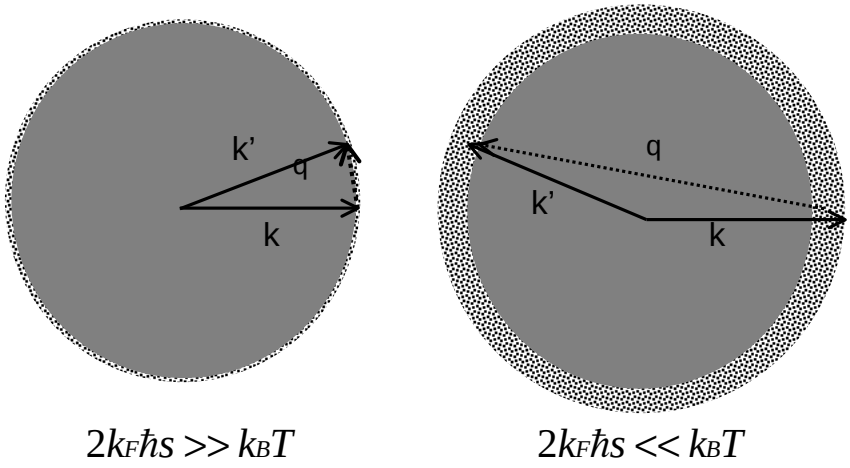

Figure 2.2: This diagram (drawing not to scale) illustrates the BG effect where for temperatures below T_{BG} the electrons participating in transport are very close to the Fermi surface. As a result of the Pauli exclusion principal, these electrons are prohibited from emitting phonons of energy that could cause large angle scattering. Above T_BG, the phase space restrictions for phonon emission is no longer prevalent and the scattering rate is dictated by the phonon occupancy function $N_q \approx k_B T$.

Acoustic phonon scattering occurs through deformation potential coupling and piezo-electric coupling (since GaAs is a polar semiconductor); the scattering matrix element for each of these couplings is stated in detail in Appendix B. Using 2.1 ,2.3 and 2.4, the temperature dependence of the mobility due to phonon scattering and impurity scattering can be calculated. In Figure 2.1 (b) is plotted the calculated mobility under equilibrium ($T_e = T_L$) taking into consideration all the various acoustic

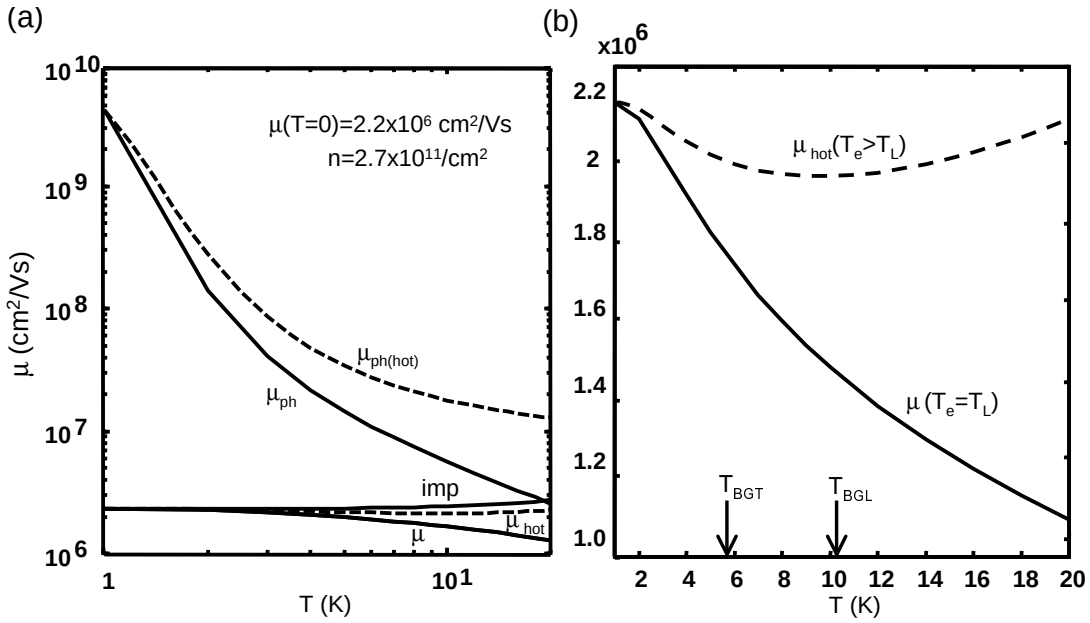

Figure 2.3: Mobility calculations for a 2DEG with density 2.7x10^{11}/cm^{-}2. The solid lines are the mobilities calculated in the case of equilibrium ($T_e = T_L$). The dashed lines indicate the calculations for hot electrons with T_L =1.5K and T_e varied from 1.5K to 20K. The impurity scattering is the same in the both cases but the phonon scattering is significantly altered. For simplicity, in (a) the mobility contributions of all the phonon scattering processes (μ_{ph}) are consolidated into one. In (b) total mobilities for the equilibrium μ and hot electron μ_{hot} cases are plotted on a linear scale.

phonon scattering processes and impurity scattering. In Figure 2.3 (a), all the phonon scattering components are consolidated into one curve and in addition the effect of hot electrons is illustrated. To simulate the effect of hot electrons, the lattice temperature T_L is pinned at 1.5K and the electron temperature T_e is varied. The total mobility in the case of equilibrium electrons does not reflect clearly the BG effect nor the $1+O(T/T_F)^2$ dependence of the impurity scattering. In the plot of the total mobility of hot electrons, however, initially a fall is seen until $T_e \approx T_{BG}$ because as T_e rises and the electrons are transitioning away from severe degeneracy, phase constraints are

alleviated and phonon emission increases. After T_e reaches T_{BG}, phonon scattering no longer increases rapidly because the phonon occupancy function is still clamped T_L is pinned to 1K; simultaneously, the rise in T_e starts to reduce impurity scattering significantly and therefore the mobility rises. The difference in hot and equilibrium mobilities is easily seen in Figure 2.3(b) which is a linear plot.

2.2.2 Energy relaxation

In calculating energy relaxation, we start with the assumption that the net energy loss rate of an an electron is equal to the energy gained from the lattice minus the energy lost from the lattice. As part of ETM, it is assumed that the net energy lost by the 2DEG $\left\langle \frac{dE}{dt} \right\rangle_{net}$ is assumed to be exactly replenished by the power supplied from an externally applied electric field P_e [29].

$$P_e = -\left\langle \frac{dE}{dt} \right\rangle_{net} = \left\langle \frac{dE}{dt} \right\rangle_{phonon+} - \left\langle \frac{dE}{dt} \right\rangle_{phonon-} \tag{2.7}$$

The differential cross section scattering rate for energy relaxation is similar to the momentum relaxation scattering rate expression discussed in the previous section. The energy relaxation scattering rate is given by

$$w_+(q,\theta) = \int_{-\infty}^{+\infty} dq_z \left|I(q_z)\right|^2 \frac{\left|C(q)\right|^2}{\epsilon^2(q_{xy}, T_e)} N_q[1 - f(E + \hbar\omega_q)] \tag{2.8}$$

for phonon absorption, and

$$w_-(q,\theta) = \int_{-\infty}^{+\infty} dq_z \left|I(q_z)\right|^2 \frac{\left|C(q)\right|^2}{\epsilon^2(q_{xy}, T_e)} (N_q + 1)[1 - f(E - \hbar\omega_q)] \tag{2.9}$$

for phonon emission. In the case of polar optical phonon (POP), $\hbar\omega_q$ is assumed to have a fixed value of 36.5meV. The energy dependent energy loss rate per electron is

given by,

$$\frac{dE}{dt} = \int_{-0}^{2\pi} d\theta[\hbar\omega_q(w_+(\theta) - w_-(\theta)] \tag{2.10}$$

and the ensemble average energy loss rate per electron is given by

$$\left\langle \frac{dE}{dt} \right\rangle = \frac{\int_{-0}^{\infty} \frac{dE}{dt} f(E) dE}{\int_{-0}^{\infty} f(E) dE}. \tag{2.11}$$

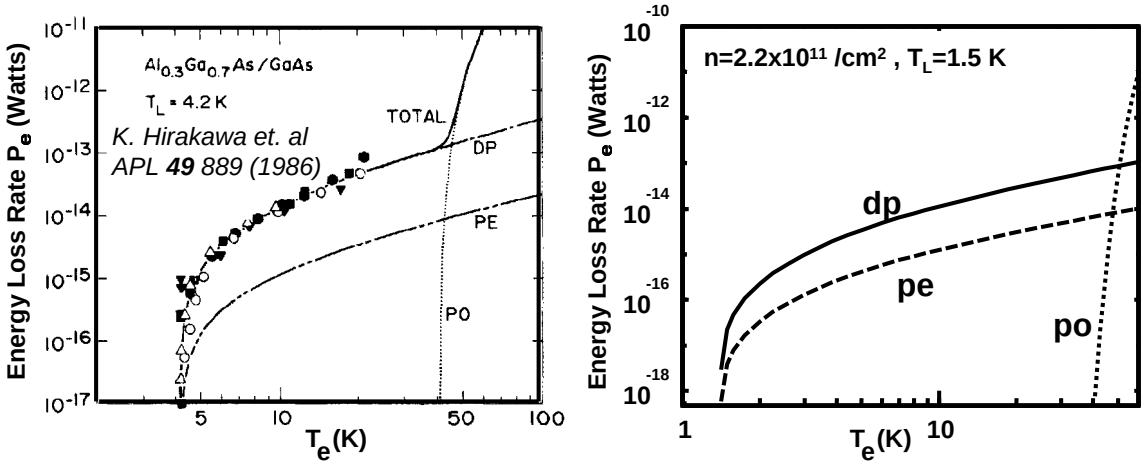

Figure 2.4: In (a) the measured data and theoretical plots for P_e vs. T_e obtained by Hirakawa *et al.* [29]. (b) Energy dissipation calculations using the model presented in this chapter for a 2DEG with density 2.2x10^{11}cm^{-}2 and a fixed T_L=1.5K.

In Figure 2.4, we see the contributions to energy relaxation from the piezoelectric and deformation coupled acoustic phonons. For T_e greater than 40K, POP scattering starts to dominate the energy relaxation process. The measured data and theoretical plots for P_e vs. T_e obtained by Hirakawa *et al* [29] are shown in Figure 2.4(a) for comparison to the calculations made using the theory presented above and plotted in 2.4(b). Hirakawa *et al* studied 2DEG samples which were held at a lattice temperature T_L =4.2K. The calculations presented in 2.4(b) are for a 2DEG sample with T_L =1.5K.

The calculations indicate that T_e rises rapidly as a function of P_e until polar optical emission sets in at ≈40K, after which energy transferred to the 2DEG is efficiently transmitted to the lattice.

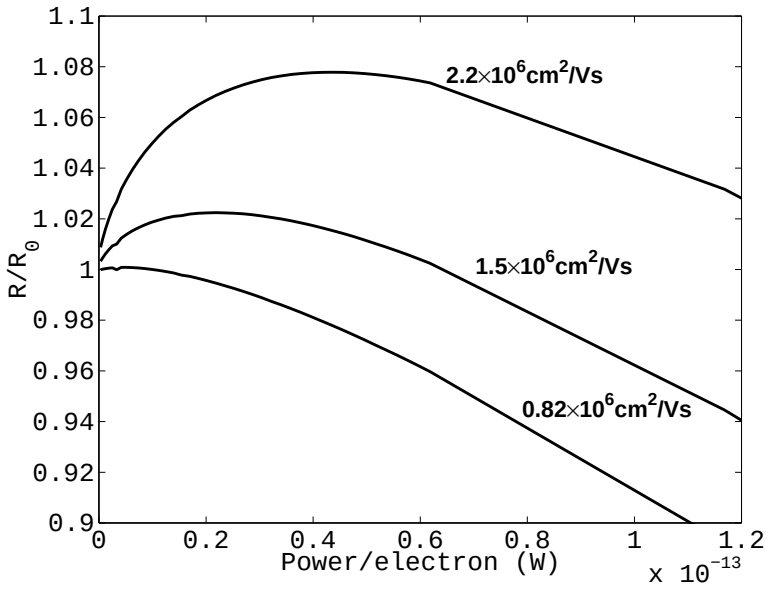

Figure 2.5: The normalized resistance R/R_0 (i.e. the resistance R normalized by the zero temperature resistance R_0) is plotted vs the Power/electron P_e. The curves corresponding to zero temperature impurity limited mobilities $\mu_I(T = 0)$ of 2.2×10^6cm^2/Vs, 1.5×10^6cm^2/Vs and 0.82×10^6cm^2/Vs. The graph clearly shows the relative importance of the BG effect on the resistance R of a 2DEG for a given $\mu_I(T = 0)$. For the sample with $\mu_I(T = 0) = 2.2 \times 10^6$ cm^2/Vs, the resistance rises by as much as 8% as a result of the BG effect. In the case where $\mu_I(T = 0) = 0.82 \times 10^6$ cm^2/Vs, the rise in R due to the BG effect is so small that it seems like R is basically a monotonically falling function of P_e. The electron density n = 2.7×10^{11}/cm^2 for all the curves.

Having calculated the momentum and energy scattering rates, it is now easy to map the power dissipation rate to the momentum scattering rate for a given T_e and T_L. In Figure 2.5, the normalized resistance for 2DEGs with varying mobility is plotted as a function of P_e assuming that T_L is fixed at 1.5K. The resistance curves

plotted are calculations for samples with zero temperature impurity limited mobilities of $2.2 \times 10^6 \text{cm}^2/\text{Vs}$, $1.5 \times 10^6 \text{cm}^2/\text{Vs}$ and $0.82 \times 10^6 \text{cm}^2/\text{Vs}$. The graph clearly shows the relative importance of the BG effect the resistance R of a 2DEG for a given $\mu_I(T = 0)$. For the sample with $\mu_I(T = 0) = 2.2 \times 10^6$ cm^2/Vs, the resistance rises by as much as 8% as a result of the BG effect. In the case where $\mu_I(T = 0) = 0.82 \times 10^6$ cm^2/Vs, the rise in R due to the BG effect is so small that it seems like R is basically a monotonically falling function of P_e. This illustrates that as expected, the BG effect diminishes as impurity scattering becomes overwhelmingly dominant.

2.3 Experiments and results

The device specifications were chosen with the intent of measuring the resistance of a hot electron 2DEG. One of the practical considerations we needed to take into account was that the Ohmic contacts to the 2DEG have resistances of $\sim$50-100Ωs, therefore large currents would cause local lattice heating in the vicinity of the Ohmic contacts, inadvertently raising T_L in an experiment where the intention is to pin T_L at a fixed value. To ensure that high current densities were achieved without Ohmic heating at the contacts, the current was supplied through large Ohmic contacts. To ensure high current densities (and thus hot electron effects), the current was channeled through a narrow wire 4μm in width defined using Schottky gates, see Figure 2.6 for an optical image and schematic of the device. The length of the device L is 150μm which is much larger than the transport length $l_m = v_f < \tau_m >$=6.4μm at the $T = 0$. Since the Schottky defined gates are known from magnetoresistance measurements to be "smooth", their presence does not add to the resistance of the device [70], therefore

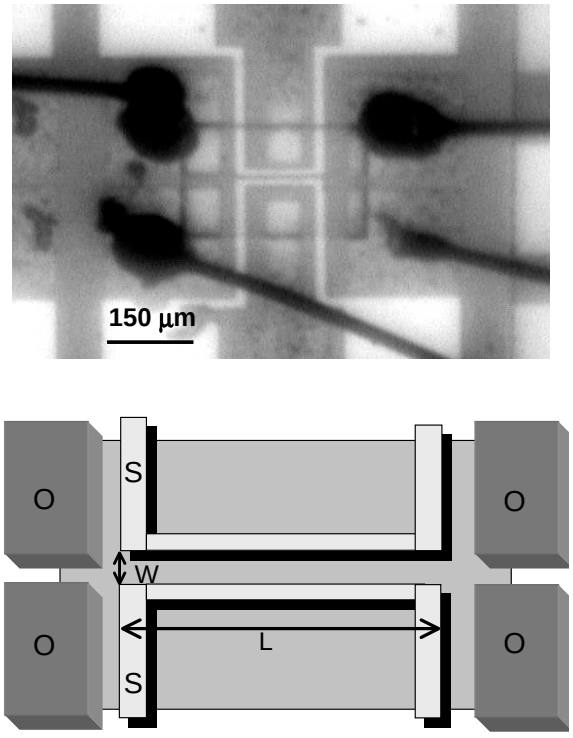

Figure 2.6: Above is an optical image of the device that was fabricated, below is a schematic of the device. A portion of the 2DEG was first isolated from the rest of the wafer by using a wet etch to define a mesa. Four Ohmic contacts were to enable four point measurement that would eliminate the resistance of the leads. The Schottky gates defined electrostatically a wire of width W=4μm and length L=150μm.

the measurements on this device were essentially "bulk" measurements made in the diffuse transport limit. We discuss the effects of rough boundaries in more detail later in Section 2.5. The details of the fabrication process are in Appendix A.

The device shown in Figure 2.6, was made from a 2DEG with a bulk low temperature mobility μ=8.2×10^{5}cm^2/Vs. A Desert Cryogenics cryogenic probe station was used to first cool the device to 1.5K and the sample temperature was then controlled

using a local heater. The electrical measurements were made using an Agilent Technologies A4156 parameter analyzer. The measured resistance as a function of bias current and lattice temperature is shown in Figure 2.7. In Figure 2.7(a) we see that

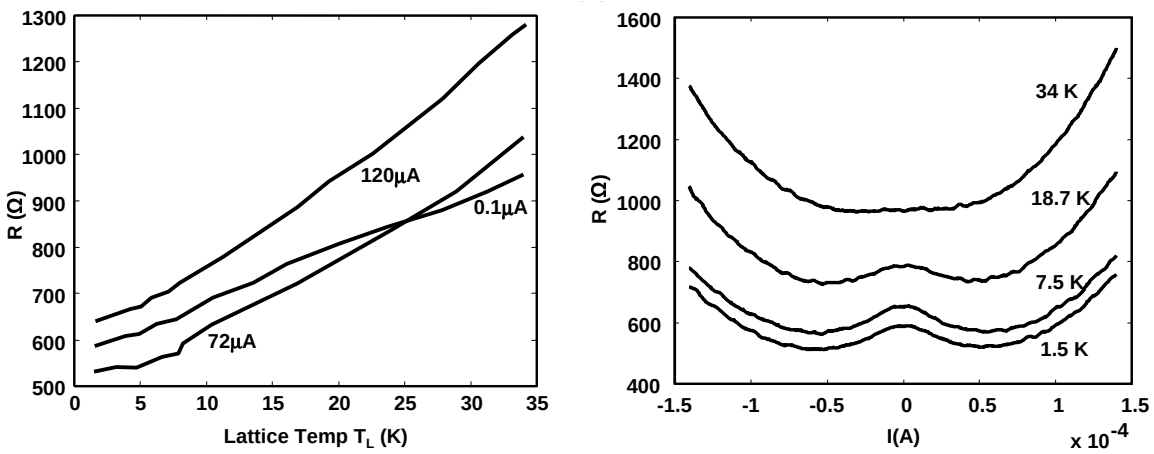

Figure 2.7: (a) Measured resistance as a function of lattice temperature T_L at bias currents 0.1μA, 72μA and 120μA. At small bias current I=0.1 μA, there is no significant electronic heating, $T_e = T_L$. At I=72 μA, $T_e > T_L$ and the resistance is smaller as compared to the resistance measured with a 0.1μA bias for $T_L < 25$ K. For I=120 μA, non-equilibrium effects set in and the resistance is higher than the I=0.1 μA case for all T_L. (b) Measured resistance as a function of bias current in a wire defined using Schottky gates at lattice temperatures T_L= 1.5, 4, 7.5, 19 and 34K. The length of the wire is 150μm and the width is 5μm. We see a pronounced peak in the resistivity around zero bias current which gradually disappears as T_L is raised.

the resistance R increases approximately linearly with T_L. For a bias current I=72μA, R is lower than as compared to when I=0.1μA for $T_L < 25K$. When I=120μA, the resistance is larger than when I=0.1μA for all T_L. The effect of reduced resistance as I is increased is seen more clearly in Figure 2.7(b), where a clear resistance peak is seen at low magnitude bias currents $|I|$ <50μA for $T_L < 34$K. In contrast to our experiments, de Jong *et al.* [20] made a measurement very similar to that described above. Their device had a width W=3.6μm and length L=127.3μm, but was made

from a 2DEG of much larger low temperature mobility μ=2.2×10^{6}cm^2/Vs. The data from Reference [20] is reproduced in Figure2.8. In this case the resistance first rises than falls, an artefact that is not seen in our sample.

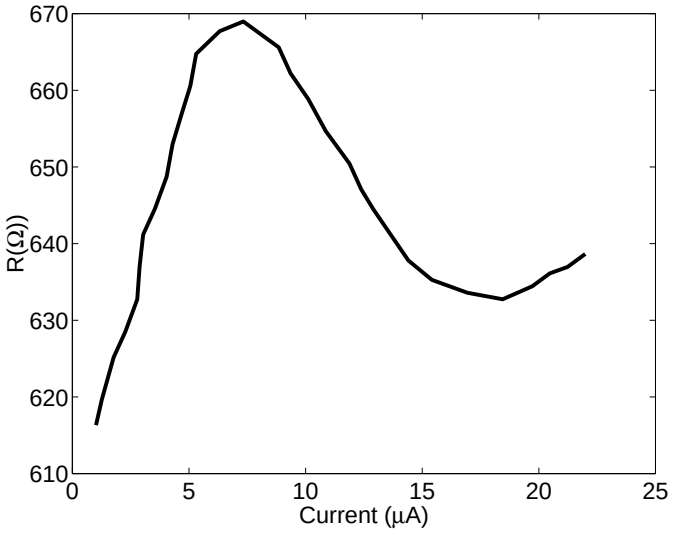

Figure 2.8: Data taken from de Jong et al. [20], shows resistance as a function of bias current in a wire defined using Schottky gates at lattice temperatures T_L= 1.5. The length of the wire is 127μm and the width is 3.5μm. We see a pronounced peak in the resistivity around at 6 μA, and then a fall as the current is further increased. The mobility of the 2DEG was stated to be 2.2×10^6 cm^2/Vs and the electron density n=2.7×10^{1}1/cm^2.

The resistance as a function of current in the two wires is qualitatively different. In order to compare our experimental results and that of de Jong et al., we plot in Figure 2.9 the normalized resistance as a function of input power per electron P_e. The experimental data and theoretical calculations using the ETM described in Section 2.2 agree fairly well. As described earlier in this chapter, the ETM model predicts that the resistance will rise rapidly as a function of T_e due to the BG effect till $T_e \approx T_{BG}$ if $\mu_I(T = 0)$ is large enough and impurity scattering does not completely dominate the momentum relaxation process. Above $T_e \approx T_{BG}$, the resistance falls as

impurity scattering reduces and phonon scattering does not increase rapidly because the phonon occupancy function remains low. In the case where μ is low to begin with, as in the case in our 2DEG, impurity scattering dominates the momentum scattering process and the BG effect is not noticeable.

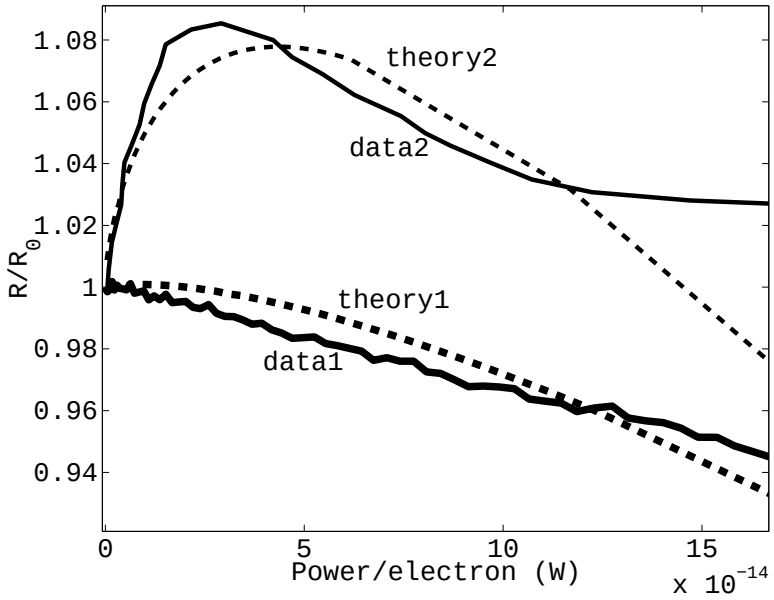

Figure 2.9: Comparison between the ETM theory (dashed) and experiments (solid) for resistance R vs Power/electron P_e. The labels "theory1" and "data1" correspond to our device, which was made from a 2DEG with a bulk mobility $\mu(T = 0)$=0.82 $\times$ 10^6cm^2/Vs and density n=2.2$\times 10^{11}$/cm2. For this sample, no resistance peak associated with the BG phenomena is seen since impurity scattering is very dominant. The labels "theory2" and "data2" correspond to the device of de Jong *et al.* [20], which was made from a 2DEG with high bulk mobility $\mu(T = 0)$=2.2$\times 10^6$cm^2/Vs and density n=2.7$\times 10^{11}$/cm2. For their sample we see a resistance peak associated with the BG phenomena since impurity scattering is less dominant and therefore the influence of the temperature dependence of phonon scattering is seen.

The results of the ETM model appear to be consistent with experimental results up to only moderately high bias currents, above which it fails. At bias currents above 50μA (and 20μA for reference [20]) the drift velocity v_d becomes much larger than

the sound velocity s, and also v_d becomes a significant fraction of the fermi velocity v_f. Under these conditions, ETM fails [40]. In the next section we briefly discuss high field transport effects.

2.4 High field transport

For room temperature bulk GaAs, intervalley scattering at electric fields $\mathcal{E}$ ∼1000V/cm destroys the linear relationship between $\mathcal{E}$ and drift velocity v_d [82]. In the case of high mobility 2DEGs at low temperatures, non-linear acoustic phonon scattering events can occur at much lower electric fields $\mathcal{E}$ ∼10V/cm, if v_d becomes significantly larger than s [40] [41].

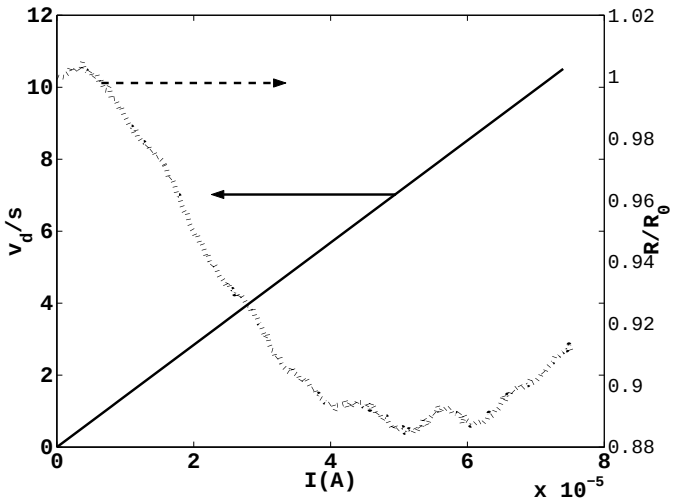

Figure 2.10: Graph of v_d/s (solid line) and R/R_0 (dashed) plotted vs. current bias for our device. The drift velocity v_d can be seen to be become significantly larger than the (longitudinal) sound velocity s as the current I increases.

In our device and in the devices in Reference [20], it is found that the resistance eventually rises at large bias currents. The ETM model does not predict this rise

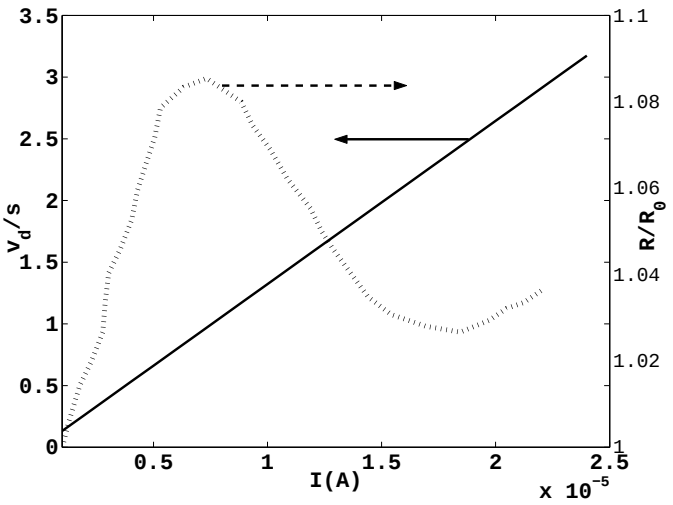

Figure 2.11: Graph of v_d/s (solid line) and R/R_0 (dashed) plotted vs. current bias for the data from [20] shown in Figure. 2.8. The drift velocity v_d can be seen to be become significantly larger than the (longitudinal) sound velocity s as the current I increases.

because some of the key assumptions are no longer met at high bias currents. The failure of the ETM model occurs when the drift velocity v_d becomes large and the finite temperature Fermi distribution cannot be used to model the electron statistics. Also, as mentioned earlier, v_d becomes significantly larger than the sound velocity s, non-equilibrium phonon effects start to play a role and also frequency dependent screening needs to be incorporated [40][41].

In Figures 2.10 and 2.11, we see that in both the sample we measured and that of de Jong *et al.*, v_d becomes considerably larger than s at the point when the resistance begins to rise again. The Green's-function theoretical approach taken by Lei and Ting [41], shows that when v_d becomes significantly larger than s, the ETM model underestimates the acoustic phonon scattering rates. Hirakawa *et al.* verify the Lie and Ting theory and the failure of the ETM model in reference [31], see Figure 2.12.

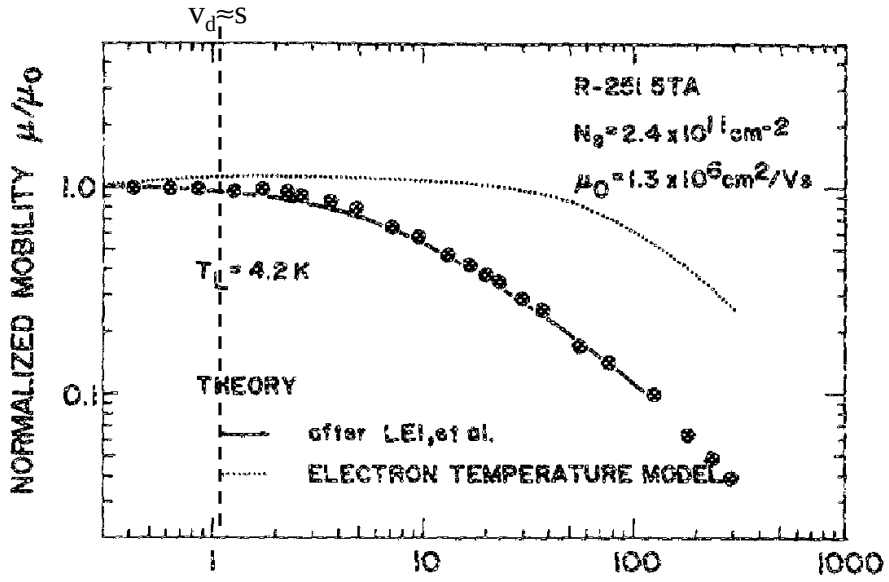

Figure 2.12: Plot of normalized mobility $\frac{\mu}{\mu_0}$ vs. electric field from Reference [31]. The dotted line is the ETM model, the solid line theory of Lei *et al.* [41], and the circles mark the measurements on a sample with n=2.4×10^{1}1/cm^2 and μ=1.3×10^{6}cm^2/Vs. At approximately 1V/cm, the drift velocity v_d approximately equals the sound velocity S for their sample (marked by vertical dashed line). We see that as v_d becomes much larger than s, the ETM model overestimates the mobility. The resistance R vs. I for the data represented in Figures 2.10 and 2.11, the electric field was varied from 0-2.4V/cm, and 0-1V/cm respectively.

Apart from high-field effects, the effect of electron-electron (e-e) scattering on the ETM model has not been considered. In the case of bulk 2DEGs e-e scattering is often ignored while calculating the classical resistance because it is a momentum conserving process. In the following section we discuss a theory proposed by de Jong and Molenkamp in [20] which states that as e-e scattering becomes large, classical hydrodynamic behavior might appear in mesoscopic 2DEG devices.

2.5 Classical size effects: boundary scattering and viscosity

A 2DEG wire with specular scattering at the boundaries should not display a classical resistivity different from that of the bulk[2]. Schottky defined gates are "smooth" (i.e. there is no significant roughness in the scale of the Fermi wavelength λ_F), as has been inferred from magnetoresistance measurements [70] and electron focusing experiments [72]. In the magnetoresistance measurements on a Schottky defined 2DEG wire [70], it was found that the magnetoresistance was negligible, which is consistent with specular reflections of electrons of the boundaries. And, in the magnetic focusing experiments where a stream of electrons was made to bend by an applied magnetic field and reflect off a Schottky defined gate, the measurements were consistent with a specular reflection model. In our experiments and in Reference [20], Schottky gates were used to define the wires, so presumably there were negligible boundary scattering size effects. It is for this reason that the analysis of Section 2.3 did not consider boundary scattering.

We now summerise the influence of boundary scattering on resistance as has been studied in the literature [22](and references there in), and then assess the case of hot-electrons flowing through a wire with "rough" boundaries. If we assume that it is possible to make completely diffuse scattering boundaries, then one could crudely estimate that the width of the wire W would set an upper bound to the momentum scattering length l_m and therefore the resistance of a wire R would be altered to

[2]The classical size effects on resistance have been studied extensively, and a good review is presented in reference [22].

$R \sim R_s(l_m/W)$ if $l_m >> W$. In reference [22], the approximate solutions to the linearized Boltzmann transport equation in the case of completely diffuse boundary scattering is derived to be

$$R = R_s(1 + \frac{4}{3\pi}\frac{l_m}{W}) \tag{2.12}$$

for $l_m/W <<1$, and

$$R = (\pi/2)R_s\frac{1}{ln(l_m/W)}\frac{l_m}{W} \tag{2.13}$$

for $l_m/W >>1$. If $l_m/W >>1$ or $l_m/W <<1$, the drift velocity should not vary substantially across the width of the wire. In the case of $l_m/W >>1$ only the electrons with momentum almost completely parallel to the boundaries will carry the vast majority of the current and therefore the velocity profile across the width of the wire would be close to constant, tapering to zero only very close to the boundaries. This regime is referred to as the "ballistic" regime and is extensively studied in the literature. If $l_m/W <<1$, then the boundary scattering does not affect the flow of current much at all so we do not expect to see any change in current density across such a wire. This is the regime in which many practical room temperature semiconductor devices function and is referred to as the "diffusive" regime. In the intermediate, or "quasi-ballistic" regime, when l_m is comparable to W, one should expect to see some structure in the current density of electrons flowing through a wire because the effective transport length would be shorter close to the wire boundaries as opposed to far away from them. However, the role of l_m is *not* the same as that of interparticle collisions which give rise to viscosity in a gas. In the length scale l_m, the velocity of an electron is randomized, and the momentum scattering events effectively transfer the momentum from the electrons to the lattice wherever they occur.

For a classical gas flowing through a pipe, the interparticle collisions alone do not contribute directly to the resistance of the pipe but do so by transferring the momentum of particles to the walls of the pipe. The interparticle collisions that are momentum conserving cause net transfer of momentum perpendicular to the flow of a gas and are the source of viscosity. In Reference [20], a theory of viscous effects in a 2DEG is presented that predicts an extremely pronounced effect on the velocity profile of electrons flowing through a wire with rough boundaries if the case of an electron-electron scattering length $l_{ee} < l_m$ *and* W is considered.

As mentioned in Chapter 1, for a classical gas, $\eta_c = \frac{1}{2}\bar{m}N\bar{v}l$, where l is the interparticle scattering length, $\bar{m}$ the mass of the particle, N the density and $\bar{v}$ the thermal velocity. The analogous expression for a electronic Fermi gas for viscosity would be $\eta_e \sim mnv_F l_{ee}$, where l_{ee} is the electron-electron scattering length [43]. In calculating the classical resistance of a 2DEG device, electron-electron scattering is normally ignored as it is a momentum conserving process and therefore does not affect the drift velocity of the electron ensemble. However, in the case of wires with rough boundaries, and width $W < l_m$, where the ratio of l_{ee}/W can be tuned, a transition analogous to transition from "ballistic" (Knudsen) to "viscous" (Poiseuille) flow in a classical gas is expected in the velocity profile of the electrons [26, 20]. In Figure 2.13 the velocity profile using the theory presented [20] is plotted. The wire was assumed to be 4μm wide and the boundaries "rough" with only 70% specular reflection. In the ballistic transport (Knudsen) regime where $l_{ee} > l_m > W$, we find that the velocity profile is flat. When l_{ee} is made smaller than both l_m and W, the Poiseuille-like flow appears and the velocity profile has a characteristic parabolic shape. If l_m is smaller

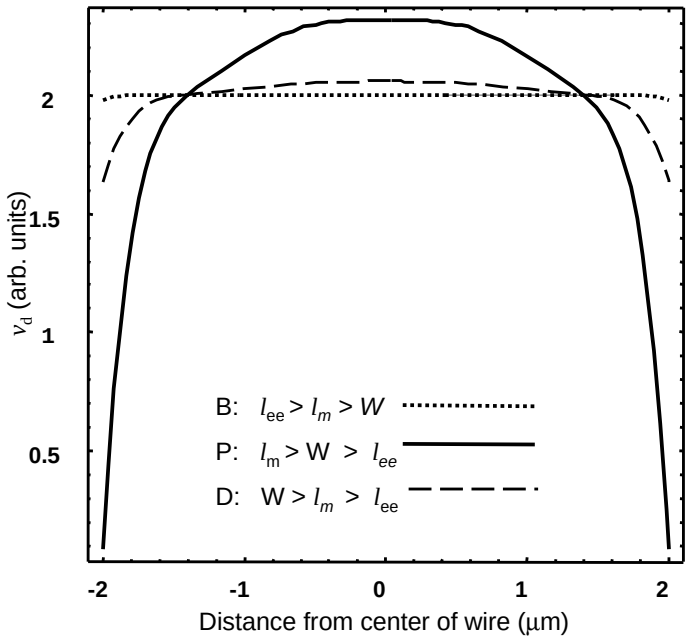

Figure 2.13: Velocity profile for ballistic (B), Poiseuille (P) and diffusive (D) transport along a wire with 'rough' boundaries. When l_{ee} becomes smaller than l_m and W, viscous flow develops and the momentum from the electrons transmitted to the rough boundaries where it is dissipated.

than W, the Poiseuille-like flow fades and the velocity profile flattens out.

In reference [70], it is shown that Schottky defined gates are more than 95% specular, where as those defined by focused ion-beam (FIB) are shown to be only 70% specular. The electron-electron scattering length $lee = v_f \tau_{ee}$ and has been measured in a 2DEG recently by LeRoy *et al.* [42], and was found to be consistent with the electron-electron scattering rate calculated by Chaplik [16], and Giuliani and Quinn [25] given by,

$$\frac{1}{\tau_{ee}} = \frac{E_F}{4\pi\hbar}\left(\frac{\Delta}{E_F}\right)^2 [ln(E_F/\Delta) + ln(2Q_{FT}/k_F) + 1/2] \tag{2.14}$$

where, $Q_{FT} = me^2/2\pi\epsilon\hbar^2$ is the Thomas-Fermi screening length and Δ is the quasi-

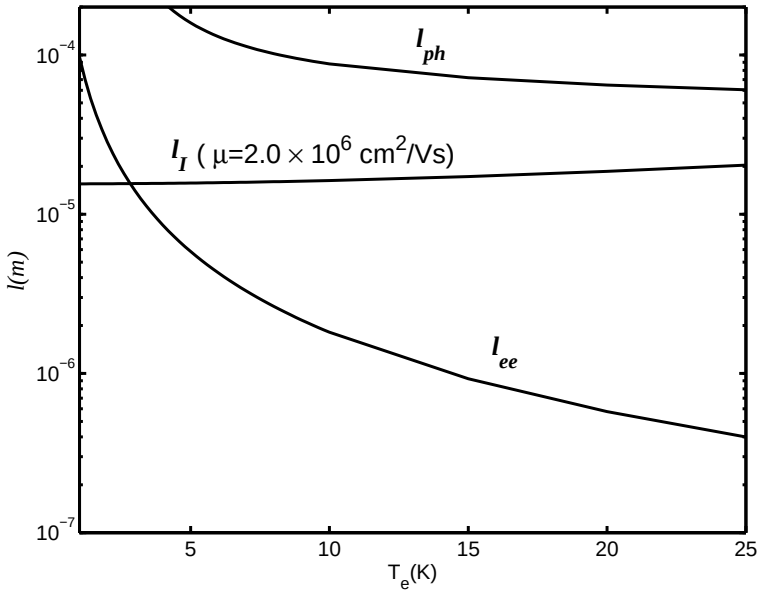

Figure 2.14: The electron-impurity (l_I), electron-phonon (l_{ph}), and electron-electron scattering lengths for a 2DEG with $\mu(T=0)$=2×10^{6}cm^2/Vs and density n=2.7×10^{11}/cm^2. The lattice temperature T_L is fixed at 1K and T_e is varied.

particle excitation energy. If we make the approximation that for electrons at temperature T_e, $\Delta \approx k_B T_e$, we can estimate the electron-electron scattering rate for a given electron temperature T_e. In Figure 2.14, the relevant scattering lengths are plotted as a function of T_e: the elctron-electron scattering length $l_{ee} = v_F \tau_{ee}$, the impurity scattering length $l_I = v_F < \tau_i >$, and the phonon scattering length $l_I = v_F < \tau_{ph} >$. In these calculations, a low temperature 2DEG mobility of $\mu(T=0)$=2×10^{6}cm^2/Vs and density n=2.7×10^{11}/cm^2 was assumed. In Figure 2.14, we see that at T_e =20K, $l_{ee} \approx 0.5\mu m$ is much smaller than l_m and if a wire with diffuse boundary scattering is fabricated with a width of $\approx 5\mu$m, then a Poiseulle-like regime as first predicted by [26] might form. In comparison to our sample, which has $l_I \approx 6.5$ μm with $\mu(T=0)$=0.82×10^{6}cm^2/Vs and n=2.2×10^{11}/cm^2, a narrower wire width W and

higher higher T_e would be needed to comfortably satisfy Poiseuille flow conditions $l_m > W > l_{ee}$.

In the transition from Knudsen to Poiseulle regimes for high mobility 2DEG wire with rough boundaries, de Jong *et al.* [20] predict a few percent change in resistance. The interplay between phonon scattering and impurity scattering described in this chapter is a bulk effect of similar magnitude and therefore it would be difficult to conclusively say whether it is one effect or the other (or both) that are occurring just by measuring resistivity alone. In our experiments and those of de Jong *et al.* [20], the specularity of reflections from the Schottky gates clearly rules out any boundary effects. The most direct way to detect any change in the velocity profile would be to "image" the currents inside a wire which has significant boundary scattering.

2.6 Conclusion

Theoretical calculations using ETM predicts the experimental results of hot electrons in a 2DEG for moderate bias currents. The conditions under which a resistance peak forms as a function of current bias in high mobility 2DEG samples were presented. This phenomena is observed only when the lattice temperature is held significantly below the Bloch-Grüneisen (BG) temperature (T_{BG}), and if the zero temperature mobility of the sample is comparable to or greater than the phonon limited mobility at T_{BG}. If these two conditions are met, then as the current bias is increased, the electron temperature rises (due to Joule heating) and the corresponding resistance rises rapidly due to the BG effect until $T_e \approx T_{BG}$. Further increasing the current bias reduces impurity scattering to a much greater extent than the cor-

responding increase in acoustic phonon scattering and therefore the resistance falls. In hot 2DEGs it is easier to detect the BG effect as compared to the equilibrium case because the rise in T_L increases the occupancy function N_q of the phonons and therefore the influence of the phonon scattering associated with opening of the phase space as T_e rises is obscured.

At high fields, the ETM model fails since the drift velocity v_d becomes much larger than the sound velocity and non-equilibrium phonon scattering effects need to be considered. Also, at high electron temperatures T_e, the electron-electron scattering length l_{ee} can be made much smaller than l_m and the characteristic length scale of a device. This raises the possibility of structure in the velocity profile of electrons flowing through a wire arising from "viscous" effects. In the next chapter we evaluate Magnetic Force Microscopy (MFM) as a tool to image these "viscous" effects.

Chapter 3

Current Sensing with MFM

3.1 Introduction

The ability to sense currents at the microscopic scale allows us to visualize and verify microscopic theories of electron transport. There is no doubt that the field of fluid dynamics has made tremendous strides because of the ability to easily image fluid flow. It is only in the past two decades, since the invention of the scanning tunneling microscope (STM) [11] and related scanning probe technologies like atomic force microscopy (AFM) [10] and MFM [48], that scientist have been able to "image" electron flow.

One of the methods developed to image electron flow in a 2DEG device involves perturbing the electron flow with a mobile Schottky gate. The gate is created by placing a negatively charged AFM tip above a 2DEG. If the tip is sufficiently charged, it is possible to completely deplete the electron gas directly below it. This perturbation to the 2DEG changes the conductance of the device being probed, and by comparing the relative effect of the tip position on the conductance it is possible to detect the paths taken by electrons flowing through the device. This method of imaging was first demonstrated by Eriksson *et al.* [23] and then further refined by Topinka *et al.* [71]. Using this technique, it has been shown that impurity scattering can create dramatic branching structures in the current flow in 2DEGS. It is unclear whether this method for imaging current flow would be suitable to detect viscous effects in a 2DEG. The perturbation caused by the tip could possibly alter the flow of the electrons significantly, especially close to the boundaries of the wire, and thereby disrupting viscous-fluid like flow to an extent that would make interpretation of the measurements difficult.

We focus on MFM as a current sensing tool, since as stated in Chapter 1, it has been demonstrated to image magnetic media at the 50 nm scale [14]. In Section 3.3, a study of the limits of the MFM current sensing technique is presented. The experiments were carried out using two different techniques, direct current MFM (DC-MFM) and alternating current MFM (AC-MFM). DC-MFM involved forcing a cantilever at the clamped end at the resonant frequency f_0 and measuring the phase change of the magnetic tip oscillation as it interacted with the magnetic field emanating from a current carrying wire. AC-MFM is a new technique, where the cantilever is not forced at the clamped end, instead the current to be sensed is oscillated at the f_0, and the amplitude and phase of the deflection of the tip is monitored. It is found that in comparing the two methods, AC-MFM is two orders of magnitude more sensitive to the currents than DC-MFM, but suffers from significantly less spatial resolution.

In using any scanning probe microscope (SPM), particularly when imaging samples close to the limits of its resolution, one has to understand the details of the probe and probe-sample interactions to be able to interpret measurements quantitatively. We begin first with the result of an experiment conducted to characterize the magnetic field produced by an MFM tip in Section 3.2, and then proceed to quantify the tip interactions with magnetic fields produced by a current carrying wire in Section 3.3.

3.2 MFM spatial resolution and tip field

The experimental results in this section were obtained in collaboration with H. Schmidt and also appear in Reference [1].

Accurate measurements of tip fields involve complex experiments that detect the Lorentz force on a focused beam of electrons that are passed close to the tip [65][49]. We exploited the known bulk magnetic characteristics of a patterned array of single domain nanomagnets (SDNMs) to measure the tip field. These SDNMs were created as a prototype ultra-high density magnetic storage media. The array consists of Ni posts with a 100 nm period fabricated using Achromatic interference lithography (AIL) and electrodeposition [64]. The posts, a scanning electron micrograph of which is shown in Figure 3.1(a), have an average diameter of 57 nm and average height of 115 nm. The sample was large enough ($\approx$1 cm^2) to produce a clear vibrating sample magnetometry (VSM) measurement and, since the period of the array was 100 nm, a typical MFM scan of 1μm^2 could measure the magnetic states of a few hundred posts. The shape anisotropy of the posts cause the easy axis to be along the long axis of the posts [64], and therefore the magnetization of the posts are always perpendicular to the plane of the wafer they are deposited on. Figure 3.1(b) is an example of an MFM scan that clearly reveals the magnetic states of the posts. The contrast in the MFM image comes from the attractive and repulsive force gradients experienced by the magnetic probe tip because of its relative magnetization to the posts. The bright regions in a scan are interpreted as an "up" state and the dark regions as a "down" state.

The VSM measurements shown in Figure 3.2 yield an average switching field of the posts $\bar{H}_{SW}$=710 Oe and a saturation moment M_s=370 emu/cm^3 [33]. We compare MFM and VSM hysteresis loops directly in Figure 3.2. MFM measurements allow the microscopic characterization of the nanomagnetic array while simultaneously provid-

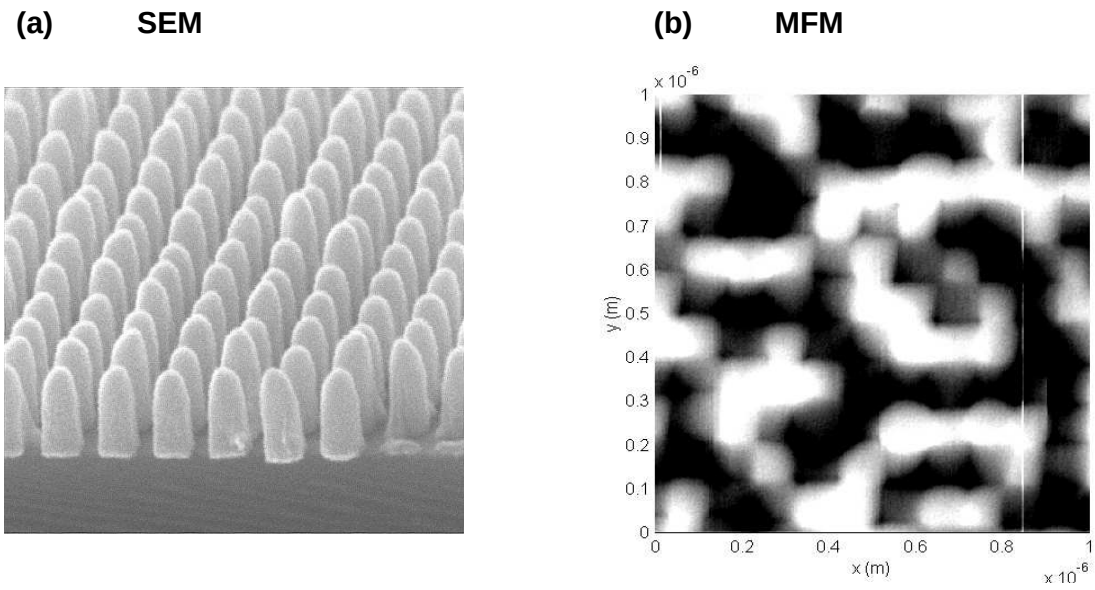

Figure 3.1: (a) SEM image of the Ni magnetic posts. The period of 100 nm corresponds to 60 Gbits/inch^2 data density. The posts are of diameter 57nm and height 115nm. (b) 1 μm^2 MFM scan of the magnetic states of the sample: "up" is white, and "down" is black.

ing topographic information when using in AFM mode. All our MFM measurements were made in a phase sensitive non-contact mode described in detail in the next section. In our experiments, we used a Digital Instruments (Dimension 3000) scanning probe microscope and model MESP-LM (magnetic force etched silicon probe - low moment) magnetic tips. An *in situ* adjustable external magnetic field H_{ext}, varying from 14 Oe to 1502 Oe, parallel to the easy axis of the magnetic posts, was applied by a movable permanent magnet mounted in a z-stage. This simple arrangement was sufficient to take successive MFM images of a fixed area of the sample for various values of external magnetic fields.

To obtain a *microscopic* "hysteresis loop" measurement, the sample was first saturated in a large magnetic field ($\gg \bar{H}_{SW}$) and then MFM scans were taken of a grid

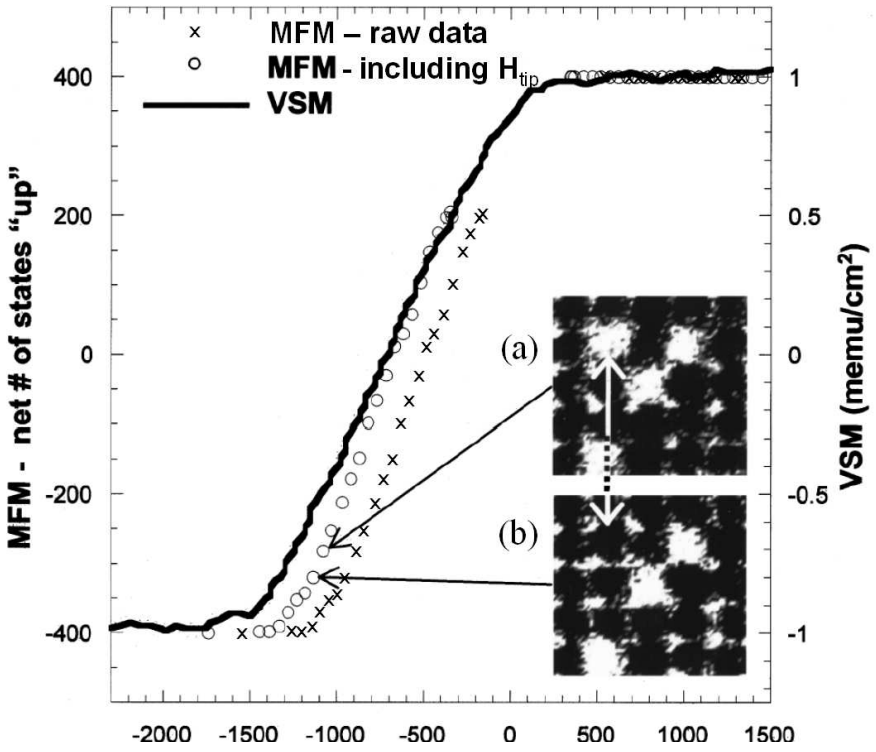

Figure 3.2: Microscopic (MFM) hysteresis curve compared to bulk (VSM) hysteresis curve. Insets (a) and (b) show a 5×5 section of the MFM data at -1080 Oe and -1136 Oe where one of the posts is seen to have switched its magnetic state from "up" (white) to down (black). The MFM data was fit to the VSM data by adding an offset of ≈ 200 Oe which corresponds to the magnetic field produced by the tip H_{tip}.

of 20 × 20 posts as the field was gradually reversed until the magnetization of all posts switched. Figure 3.2 shows the microscopic hysteresis loop recorded by keeping track of the magnetic states of each element in the grid as a function of incrementally increasing applied magnetic field. The raw data in which we do account for the tip field H_{tip} is marked with crosses. If H_{tip} is assumed to be ≈200 O and the MFM data is offset accordingly (shown as open circles on the graph), it agrees fairly well with the VSM measurement (dark solid line).

There is a gap in the data between +200 Oe and −200 Oe because we were not able

to eliminate the effect of the stray magnetic field, H_{tip}, produced by the tip and the discrepancy between the two curves, namely the relatively smaller slope (dM/dH) for the VSM data, can be explained by the fact that the MFM measurements detect just the magnetic state (up or down) rather than the actual magnetization of each post. The magnetization of the posts are probably not all fully saturated perpendicular to the plane of the sample because of variations in shape and orientation of the crystal axis, and interactions from neighboring particles.

The quantitative agreement between MFM and VSM measurements provides an important unprecedented corroboration of the macroscopic collective behavior of the nanomagnets with a microscopic measurement [1]. The unique information gained from MFM measurements is the microscopic map of the individual switching fields. This map gives us the magnetic configuration of the neighboring states as the elements flip. Thus we are able to account for the interaction of the neighbors in determining the switching field of each element by calculating the total interaction field from the neighboring nanomagnets using magnetostatics. Figure 3.3 shows the standard deviation of the average switching field ΔH_{SW} as we account for the interaction fields from 4,8,12,20 and 24 neighbors. Previously, ΔH_{SW} was determined from a fit parameter to the VSM hysteresis loop with relatively large uncertainty [33]. The inset in Figure 3.3 shows the distribution of switching fields by taking into consideration (a) no interactions (b) the interactions from 24 nearest neighbors. The effect of the long range interactions is clearly seen in Figure 3.3. The apparent standard deviation in switching fields starts at $\Delta H_{SW} = 276$ Oe, the value obtained without considering the effect of interactions, and steadily falls as we include the interaction fields of

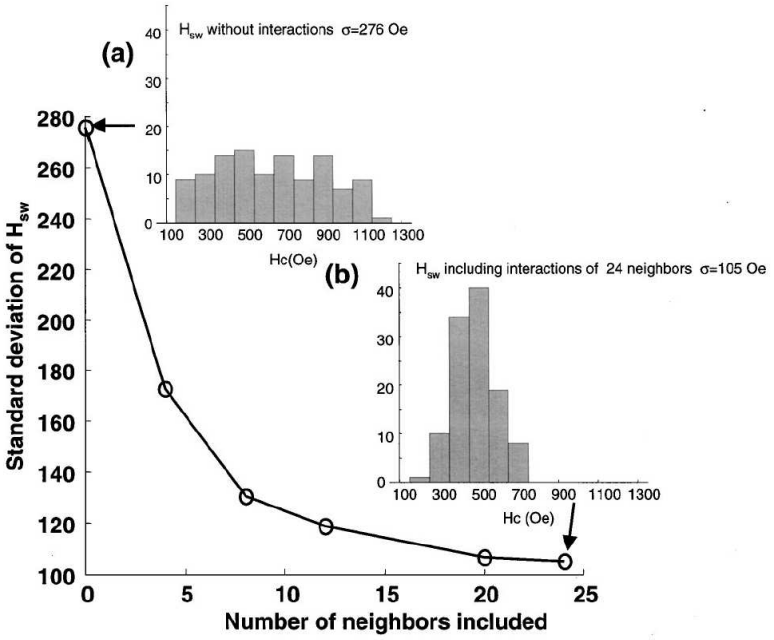

Figure 3.3: Standard deviation of switching fields vs. number of neighbors included in calculating the switching field. Inset (a) distribution with no nearest neighbor interactions, inset (b) distribution with 24 nearest neighbor interactions.

more and more neighbors eventually plateauing only after accounting for 24 nearest neighbors to a value of $\Delta H_{SW} = 105$ Oe. The actual values for ΔH_{SW} are probably larger than the recorded values as we were not able to scan the external magnetic field through the range -200Oe to $+200$Oe, a range over which 22% of the posts flipped. Though this is a significant error, it is a consistent one and does not alter the trend shown in Figure 3.3.

In summary, we have investigated the switching field behavior of single domain nanomagnets in a dense array. By using MFM, it was possible to spatially resolve the hysteresis loops of individual nanomagnets. The magnetostatic interactions play

an important role, and up to 24 nearest neighbors need to be taken into account in determining the switching field distribution. More significant to our goal to image currents, we were able to verify that MFM is able to measure magnetic signals with sub-100nm spatial resolution. And, the stray tip magnetic field $H_{tip} \approx 200$ Oe was measured in a novel manner by taking advantage of the known bulk behavior of the patterned array of nanomagnets. McVitie *et al.* in Reference [49], measured $H_{tip} \approx 400$Oe for a regular MESP tip. We used MESP-LM tips that are designed to have a lower magnetic moment by having only half the thickness of magnetic thin film material (CoCr) deposited on it compared to the MESP model [1]. Therefore, our measurements of $H_{tip} \approx 200$ Oe seems to be consistent with the results of Reference [49].

In the next section we quantify the interaction of the MFM tip with the fields emanating from a current carrying wire. The wire is metallic and its shape is well defined, and by assuming that the current flows uniformly through the wire the magnetic field interacting with the MFM tip can be precisely calculated. We find that the response of the tip to DC currents is qualitatively different from that of AC currents.

3.3 Determining current resolution

The experimental results in this section were obtained in collaboration with M. H. Wang and also appear in Reference [78]. The numerical simulations of the cantilever response was generated using software written by M. H. Wang.

[1] This was learnt through private communication with Digital Instruments, the tip vendor.

3.3.1 Cantilever model

The point-mass model (PMM) is often used to model scanning probe dynamics[63], and is sufficient in most applications of MFM as well. However, we need to use the full beam equation to model the cantilever dynamics because it allows us to introduce the necessary boundary conditions that accurately describe our experiments. The beam equation for a cantilever, with moment I, Young's modulus E, density ρ, cross-sectional area A and damping factor γ, is given by [59]:

$$EI\frac{d^4z}{dx^4} + \gamma\rho A\frac{dz}{dt} + \rho A\frac{d^2z}{dt^2} = 0 \tag{3.1}$$

The variable x is the distance along the length of the cantilever and z is the variable that tracks the deflection of the cantilever, see Fig.3.4(b). By making the assumption that the solution has the form $z(x,t) = Z(x)q(t)$, one can solve equation (3.1), given sufficient boundary conditions [21].

In the case of DC-MFM, the cantilever is driven at a set frequency, ω_d at $(x = 0)$, with an amplitude A_d. Further, the slope of the cantilever at $x = 0$ is zero, because the beam is clamped to the moving piezotube. Also, because the beam ends at $x = L$, there cannot be curvature at that point. The last boundary condition which sets the value of $\frac{d^3z(x=L,t)}{dx^3}$ relates the shear force at $x = L$ to the tip-sample interaction force. In the presence of a device carrying DC current, the tip-end of the cantilever experiences an attraction or a repulsive force in the z-direction, perpendicular to the sample provided the magnetization of the tip is in the z-direction. This force $F(z)$ can be expanded into a Taylor series:

$$F(z) = F(z_0) + \frac{\partial F}{\partial z}|_{z_0}(z - z_0) + \frac{1}{2}\frac{\partial^2 F}{\partial z^2}|_{z_0}(z - z_0)^2 + ... \tag{3.2}$$

The first term shifts the equilibrium position of the cantilever beam at $x = L$. The deflecting force around the equilibrium can be approximated by the second term, which is represented as an effective spring with stiffness k^*[58], where:

$$k^* = \frac{\partial F(z)}{\partial z}|_{z_0} \tag{3.3}$$

Therefore, the four boundary conditions that we need in order to model the cantilever dynamics, are given by:

$$z(x = 0, t) = A_d e^{\jmath \omega_d t} \tag{3.4}$$

$$\frac{\partial z(x = 0, t)}{\partial x} = 0 \tag{3.5}$$

$$EI \frac{\partial^2 z(x = L, t)}{\partial x^2} = 0 \tag{3.6}$$

$$EI \frac{\partial^3 z(x = L, t)}{\partial x^3} = k^* z(x = L, t) \tag{3.7}$$

It is important to note here that A_d is typically in the sub-angstrom range and is "amplified" such that the tip end of the cantilever oscillates with an amplitude $|Z(x = L)| \approx 10$nm. The amplification is approximately equal to the Q of the system. The tip-sample interactions for currents in the milliampere range being sensed using DC-MFM cause only minute change in the relative tip amplitude $\left(\frac{\Delta Z}{Z}\right)_{x=L} \approx 10^{-3}$, which is hard to measure. However, the corresponding change in phase of the tip oscillation $\Delta\phi$ (which increases linearly with current) is a few degrees, and is easily detected using a lock-in measurement.

In the case of AC-MFM, the cantilever is not driven at the clamped end ($x = 0$), i.e. $A_d = 0$, but by the magnetic force term that acts at the tip ($x = L$). Therefore, the zeroth order term $F(z_0)$ can no longer be neglected. Furthermore, it is orders of magnitude larger than the higher-order terms which can be ignored. The boundary

conditions for AC-MFM are therefore given by:

$$z(x=0,t)=0 \tag{3.8}$$

$$\frac{\partial z(x=0,t)}{\partial x}=0 \tag{3.9}$$

$$EI\frac{\partial^2 z(x=L,t)}{\partial x^2}=0 \tag{3.10}$$

$$EI\frac{\partial^3 z(x=L,t)}{\partial x^3}=F_z(z_0)e^{j\omega_c t} \tag{3.11}$$

where ω_c is the current frequency, $F(z_0)$ is the same Taylor series component as in the DC case, and z_0 is the effective tip-sample distance.

The amplitude of tip oscillation $|Z(x=L)|$ increases linearly with current. In our experiments described below, currents in the milliampere range induce oscillations with $|Z(x=L)|$ ≈1nm, which is easily detected. In contrast to the phase response in the case of DC-MFM, which is typically only a few degrees and is proportional to the gradient of the magnetic force interaction, the phase-response in AC-MFM undergoes a π phase shift as the tip is scanned across a current carrying wire because of the change in sign of the magnetic interaction force. For AC-MFM, the information contained in the phase response of the cantilever is the direction of the current, and the amplitude response contains the magnitude of the current. Further, if we use the extended monopole model discussed below, we conclude that the cantilever amplitude responds proportionally to strength of the magnetic field in AC-MFM, and the cantilever phase responds to the gradient of magnetic field in DC-MFM.

3.3.2 Tip-sample interaction model

The force on a tip due to the magnetic field of the sample can be represented as a convolution between the probe moment and the sample stray field. Models describing the magnetic force on hard magnetic tips, where the magnetization of the sample and the tip remains undisturbed during the scanning process, have been investigated experimentally [6]. The point dipole approximation, first proposed by Mamin et al. [47], describes the tip as an ideal dipole, with magnetic dipole moment $\mathbf{m}$. A slightly more complicated model describes the tip as the sum of an ideal monopole and an ideal dipole, where the monopole is an approximation of an elongated dipole. The force experienced by the tip due to magnetic field is,

$$F = \mu_0(q + \mathbf{m} \cdot \nabla)\mathbf{H} \tag{3.12}$$

where q is the magnetic monopole moment of the tip and $\mathbf{H}$ is the magnetic stray field from the sample[28].

Several groups have experimentally determined the effective values of q and $\mathbf{m}$ for various MFM tips [6], [60]. Kong et al.[38] took advantage of the well defined magnetic field produced by microfabricated current carrying rings to calibrate the magnetic moments of tips. They presented values for the monopole (2.8×10^{-6} emu/cm) and dipole (3.8×10^{-9} emu) moment of a tip covered with 65 nm cobalt film for a current ring with 5μm diameter and found that the dipole moment value when using a 1μm diameter ring is about one order of magnitude smaller. Lohau et al.[44] explained the difference between the two rings by relating a characteristic decay length of the magnetic field to an effective volume of the magnetic tip that is actually interacting with the field. They concluded that the usage of the point probe approximation needs

to be adjusted by an effective distance, δ, above the tip apex, because the location of the point probe within the real physical tip depends on the magnetic stray field. Similar observations have been made by Mamin et al.[47] for the dipole model and Belliard et al.[8] for the monopole model. Fig. 3.4 shows the schematic of the extended point probe model. The lift height, d, is a fixed distance between the end of the tip and the sample that is set before each scan, and the point probe is "effectively" at a height $z = d + \delta$ above the sample.

Lohau et al. also determined that "an *unambiguous* MFM-image analysis can only be performed when using *either* the monopole *or* the dipole contribution of the magnetic tip." [44]. Similar conclusions were made by van Schendel et al.[32], [73], who used transfer functions in the Fourier domain to quantify the magnetic force on the tip. When compared to the point-pole tip models, the authors found the extended monopole model to agree best with their simulations. While the dipole and monopole models only match the experimental data at specific spatial wavelengths of the sample's magnetization, the extended monopole model matched over a greater range of wavelengths. In this section, only the extended monopole model is considered, unless specified otherwise. In this model, the magnetic monopole q is assumed to be at an effective distance of $z = d + \delta$, see Fig. 3.4(c). Also, since only the cantilever movement in the z-direction is measured, equation (3.12) is reduced to,

$$F_z = q\mu_0 H_z. \tag{3.13}$$

This means that the magnetic force is proportional to the magnetic field. Therefore, the magnitude of the deflection in AC-MFM is proportional to the magnetic force and the phase response in DC-MFM is proportional to the gradient of the force in

the z-direction.

3.3.3 Experiments and results

The experimental setup for DC current sensing is shown in Fig. 3.4(a). A 2μm wide 200nm high metal wire fabricated on a silicon dioxide insulator was the device that carried the current sensed using MFM. We used a Dimension 3000, Digital Instruments SPM along with MSEP-HM tips for all our experiments. The data acquisition was performed external to the SPM. From the SPM's signal access module, the signal proportional to the amplitude deflection was fed to a Stanford Research Instruments SRS844 lock-in amplifier which had as its reference signal either the piezotube drive signal for DC-MFM, or the current drive signal for AC-MFM. The data sampling rate of the lock-in was set at 32 Hz and the time constant was at 30 ms. The value of Q was found experimentally by the equation $Q = f_0/\Delta f_0$ where f_0 is the resonant frequency and Δf_0 is the half-width frequency. The tips used had Q's of approximately 180$\pm$10.

In the DC-MFM technique, a cantilever driven at its resonant frequency was scanned over the current carrying wire at a height of 200nm. DI instrument uses the LiftMode technology to sense long-range forces, such as electrostatic and magnetic forces. LiftMode allows the tip to first perform a topographical scan across the sample, in which the tip is positioned close to the sample surface and amplitude feedback is used to extract the topographical makeup of the sample. Once topography is known and stored into memory, the tip rescans across the sample at a fixed distance above the topography to ensure that the tip is responding predominantly to the long-range

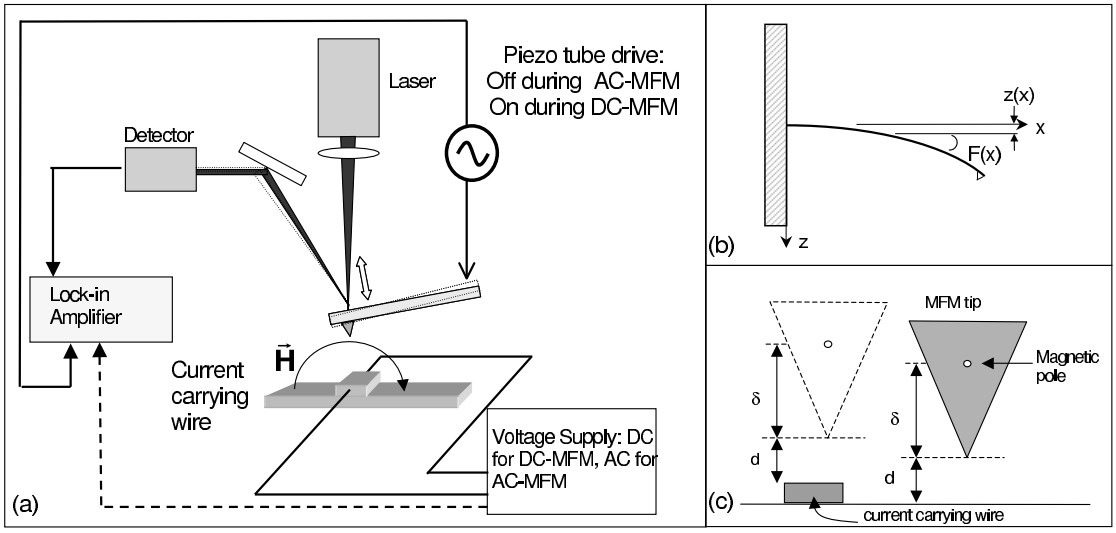

Figure 3.4: (a) MFM setup for AC and DC-MFM current sensing. For DC-MFM, a sinusoidal signal drives the cantilever at frequency ω_d and provides the reference signal for the lock-in, while a DC current is sent through a wire. In AC-MFM, the cantilever is driven by the interaction between the magnetic tip and the magnetic field produced by an oscillating current in the wire. The input signal to the lock-in is taken from the photodetector signal of the AFM. (b) Diagram (not to scale) showing illustrating the coordinate system and variables. (c) Schematic of the extended point probe model.

forces and is minimally contaminated by the topography. Figure 3.5(a) shows the raw data acquired by the lock-in of the phase response of the cantilever. The total phase response results from the combined electrostatic, topographic, and magnetic interactions. However, because of the geometry of the experiment and direction of the current in the wire, we know that the magnetic interaction between the tip and sample should be anti-symmetric across the axis of the wire. This is because the tip magnetization is in the 'z' direction and the 'z' components of the magnetic field on either side of the wire have opposite direction and equal magnitude. Using this

geometric argument, we extract the odd component of the data (about the wire axis), shown in Figure 3.5, and attribute this part of the data to the magnetic interaction. The even part of the data we do not consider in this paper, as we assume it contains artifacts due to topographic and electrostatic interactions.

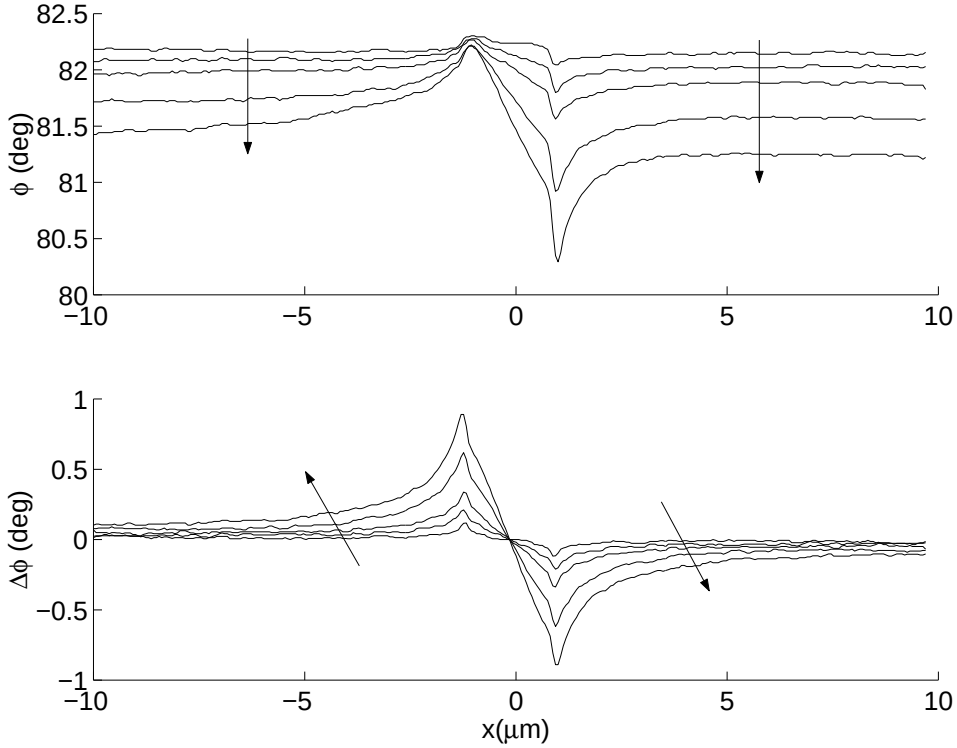

Figure 3.5: The experimental data of the cantilever phase response to a 2 μm-wide wire carrying 1,3,5,10 and 15mA of current, at a lift height of 200nm. The arrows point in the direction of increasing current. The top set of graphs represent the raw data and the bottom set, the odd component of the raw data. It is assumed that since the z component of the magnetic field is antisymmetric about the center of the wire, the entire phase response related to the magnetic interaction is contained in the odd component of the data.

The extended monopole and dipole models are both compared to the experimental results with 15 mA DC current in Figure 3.6. For the extended monopole model, q and δ are fitted to match the experimental results. The values obtained for q and δ

are 1.9×10^{-7} Am and 650 nm, given that the lift height is 200 nm. The experimental and simulated results are closely-matched, particularly within the the width of the wire, which is between x = -1μm and x = 1μm. Further away from the wire, the experimental results fall off slower than the simulations. This is possibly due to the geometry of the tip, which is not simulated in the model. As the tip moves away from the wire, the outer rim of the pyramidal tip may still interact with the magnetic field, causing some phase response. The extended dipole model simulation agrees less-well with the experimental result. In the best fit, m_z and δ are found to be 2.5×10^{-13} Am^2 and 1000nm, respectively. Away from the edge of the wire, the phase response of the extended dipole model falls off faster and even overshoots a little before approaching zero. Therefore, it appears that the extended monopole model better represents the magnetic tip-sample interaction.

The increased phase response due to greater current is evident in Fig. 3.5. The maximum phase response is linearly related to the current as is shown in Fig. 3.7. The line-fit to the experimental data yields a slope of 0.12 deg/mA. A noise floor of our phase measurement is at $\approx$0.2 degrees, this sets the current sensing limit for DC-MFM at 2mA.

In the AC current experiments the piezotube drive amplitude and frequency are both set to zero, leaving the AC magnetic field as the only driving force. The current is driven externally by the function generator at frequency ω_c. The sync output from the function generator provides the reference signal for the lock-in amplifier. The vertical deflection signal is taken from the photo-detector output and fed to the lock-in as the input signal. The experimental tip response to varying AC currents is shown

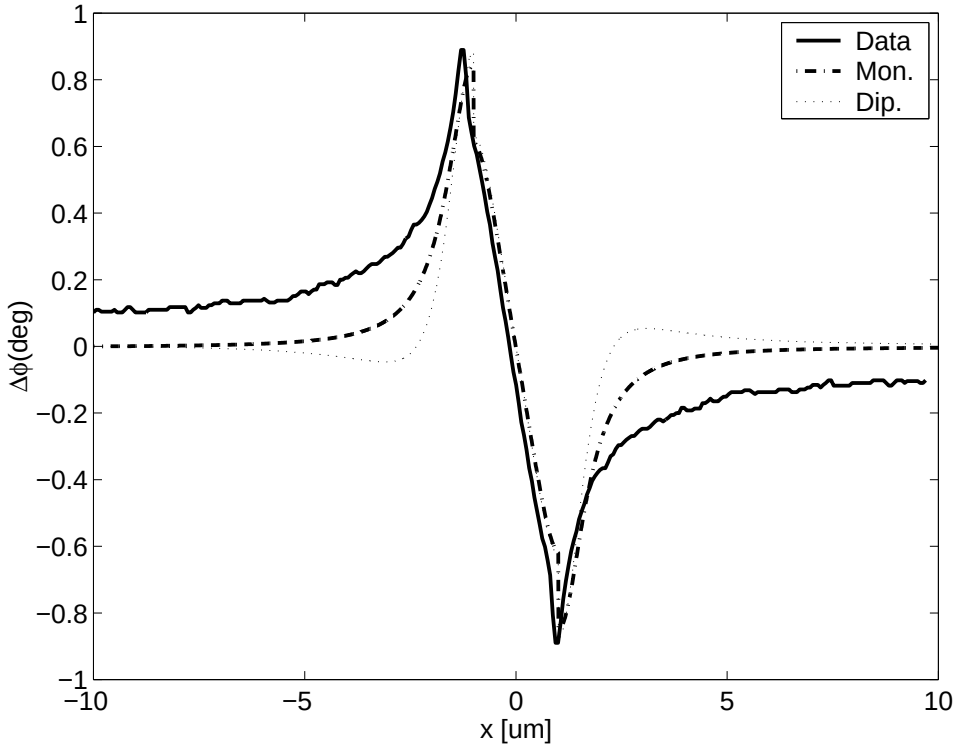

Figure 3.6: Comparison between the experimental and simulated results of the cantilever phase response to a 2 μm-wide wire carrying 15 mA DC current. The best fit extended monopole model that describes the magnetic tip-sample interaction has $q = 1.9\times10^{-7}$ Am and $z = 850$ nm for the magnetic moment and effective lift height. The best fit extended dipole model has $m_z = 2.5\times10^{-3}$ Am^2 and $z = 1200$ nm for the magnetic dipole moment and effective lift height.

in Fig. 3.8. As in the DC experiments, the same wire is used and the lift height was fixed at 200 nm and the wire is 2 μm-wide, centered at $x = 0$. A 180-degree shift in the phase response is observed as is expected. The offset in the actual experimental phase values could be due to the AFM's internal circuitry or delay between the photodetector output signal to the lock-in.

In order to effectively visualize the data, we incorporated the magnitude and phase response curves into a single curve, as shown in Figure 3.9. For the data values in

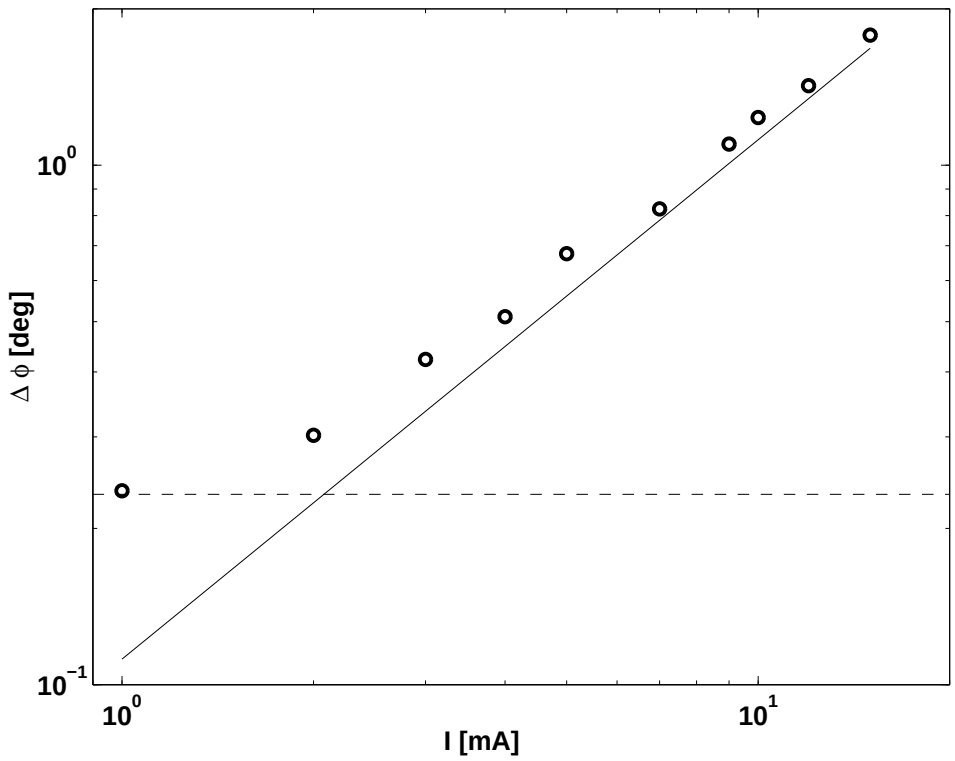

Figure 3.7: The relation between the maximum phase response and current in the DC-MFM data is plotted. The relationship is linear with a slope of 0.12 deg/mA for points above the noise floor, which is marked with a dotted line. The noise floor sets the DC-MFM sensitivity to 2mA

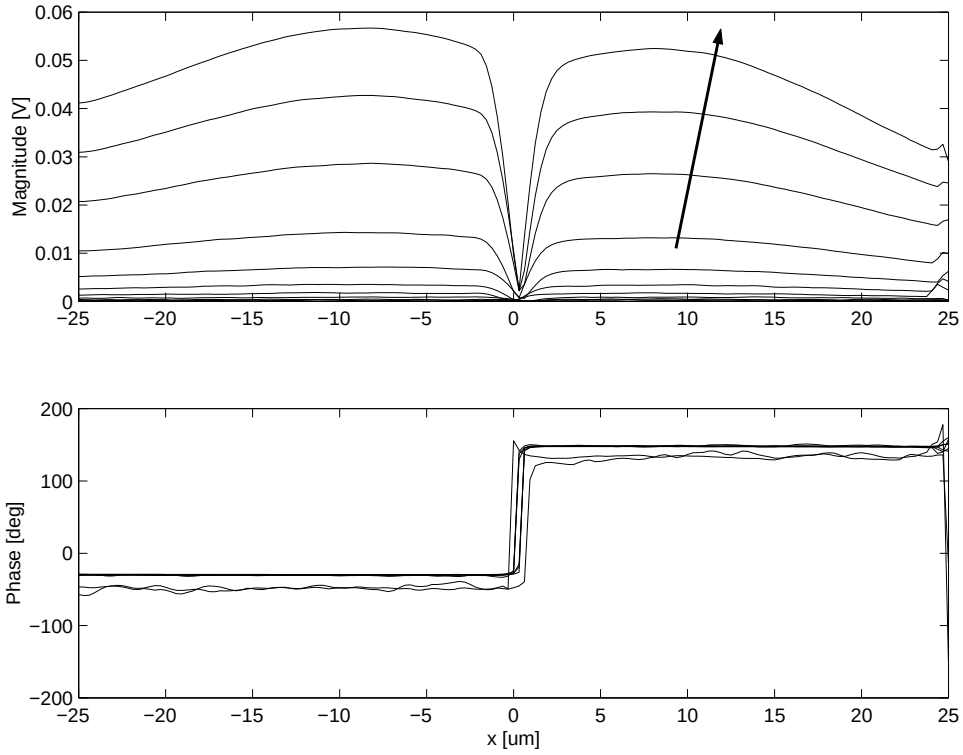

Figure 3.8: Experimental magnitude and phase responses to varying AC current through a 2μm-wide wire centered at $x = 0$. The cantilever is driven on resonance. Current levels are 5, 25, 50, 100, 250, 500 μA and 1, 2, 3, 4 mA. The arrow is drawn in the direction of increasing current. Tip-sample distance was 200 nm. The amplitude is measured from the photo-detector which outputs a voltage. Calibration measurements indicate that 1mV$\approx$1nm

these curves, the positive data points are 180 degrees out of phase with those that are negative. Once again, we extract the odd components of these curves as we did with the DC phase response data, with the understanding that all symmetric contributions were either from topographic or electric interactions between tip and sample.

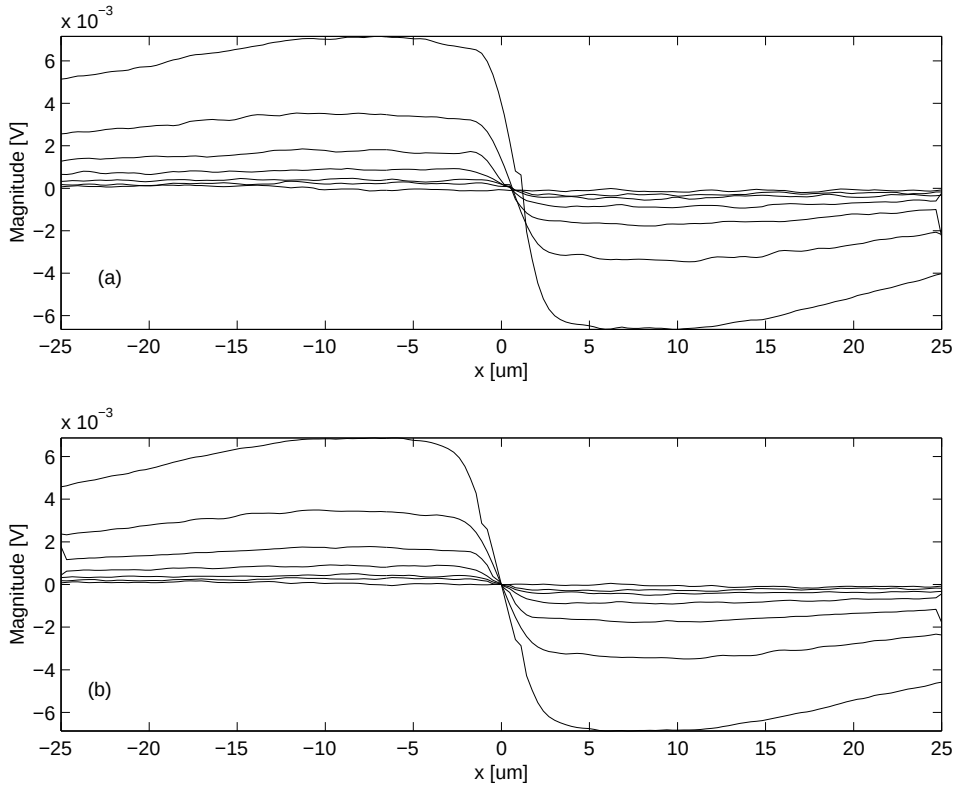

Figure 3.9: The magnitude and phase data is incorporated into a singe curve. Data values in the plot that are positive are 180 degrees out of phase with those that are negative. The plots are for from current levels are 5, 15, 25, 50, 100, 250, and 500 μA. The responses increase with current. Tip-sample distance was 200 nm. (a) is the raw data and (b) is the odd component of (a). As in the DC response, the magnetic field response of the cantilever should be entirely anti-symmetric.

The experimental amplitude data is in units of voltage, as it is taken directly from the output of the photo-detector. Through a calibration routine, we were able to estimate the relation between the photo-detector signal and actual tip deflection.

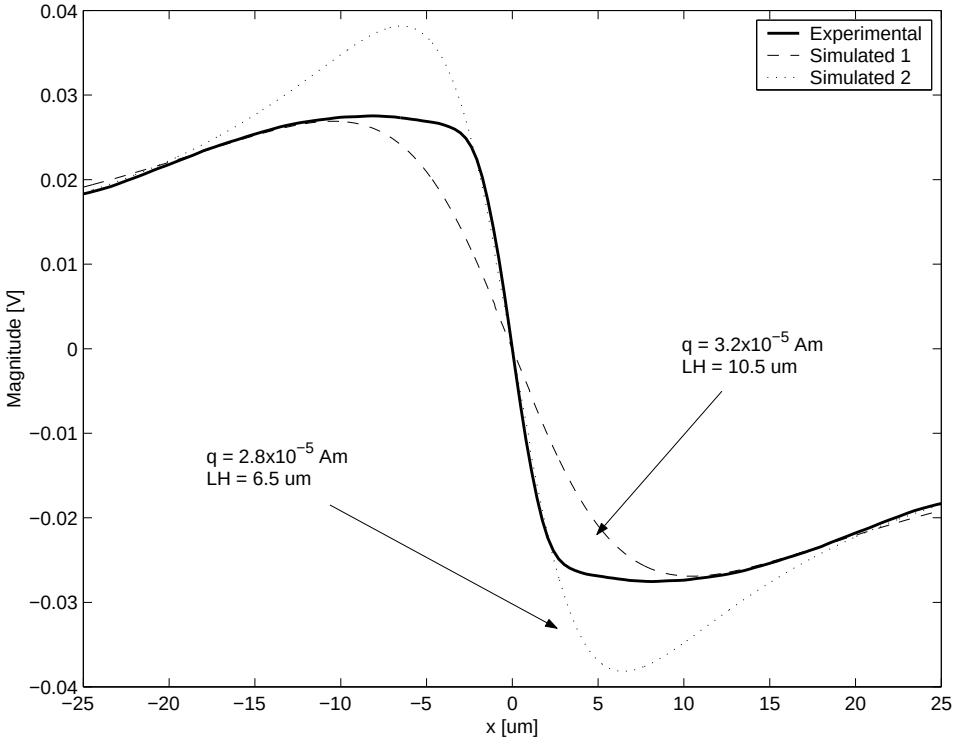

Figure 3.10: Comparison between the experimental and simulated results of the cantilever magnitude response to a 2 μm-wide wire carrying 2 mA AC current. The current frequency matches the first vibrational resonance of the cantilever beam. The simulation used the extended monopole model to describe the magnetic tip-sample interaction. Two fits were used to match the experiment. The first yields $q = 3.2\times10^{-5}$ Am and $z = 10.5$ μm and the second has $q = 2.8\times10^{-5}$ Am and $z = 6.5$ μm.

This conversion varies with each measurement session because the tip placement and laser alignment differ from session to session. For the data shown, we were able to estimate that 1 mV corresponded to $\approx$1 nm deflection. In Fig.3.10, the experimental and simulated magnitude responses to 2 mA AC current are shown. The simulations assume the extended monopole model. The data plotted with a dashed line uses the parameter values $q = 3.2\times10^{-5}$ Am and $z = 10.5$ μm, and the dotted uses $q = 2.8\times10^{-5}$ Am and $z = 6.5$ μm. For the theoretical simulation in which the effective

lift height is 6.5μm, the agreement to experiment is better further away from the center of the wire. When the larger lift height of 10.5μm is assumed, the comparison to experimental data is best directly over and immediately close to the wire. The need for two fits may be because the magnetic field decays faster as a function of tip-sample distance near the wire.

Using AC-MFM, our measurement apparatus is able to sense currents that are more than two orders of magnitude smaller than when we use the DC-MFM technique. In Fig.8, the maximum amplitude response is plotted for different current values. The signal AC-MFM sensitivity is 1.5mV/mA, and a noise floor of 0.1mV allows us to detect currents down to 15μA. It is easy to understand that in the case of AC-MFM, since we excite the cantilever at its resonance frequency, we are able to exploit the mechanical gain of the system which occurs on resonance. Therefore, we are able to detect currents that are roughly a factor of Q smaller. The extended monopole model used to simulate both the DC-MFM and AC-MFM results used vastly different values for effective monopole q and lift height δ. The values for δ differed by an order of magnitude and the q values by two orders of magnitude. Further investigation is needed to understand the large differences in these two fitting parameters that are used when modeling the two techniques.

3.4 Conclusion

Using the AC-MFM technique it is possible to measure currents that are two orders of magnitude smaller than what can be detected using the more conventional DC-MFM method. The enhanced sensitivity occurs in the AC-MFM technique because

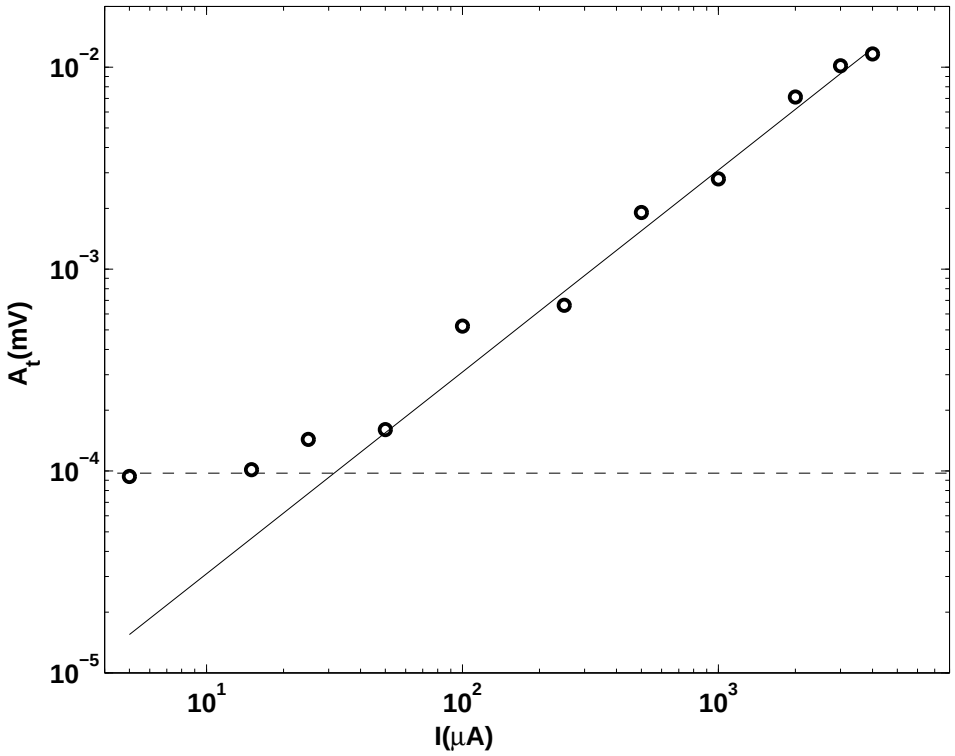

Figure 3.11: The maximum amplitude response to various AC current values is plotted. The data points form a linear relation with a slope of 1.5mV/mA, until the noise floor of 0.1mV is reached.

it takes advantage of the mechanical gain that occurs when the cantilever is forced at its resonance frequency. Therefore AC-MFM places MFM magnetic sensitivity with respect to oscillating magnetic fields in the 10μT range. The experimental data matched reasonably well with the theoretical calculations [78]. The theoretical model accounted fully for the physical characteristics and conditions of the cantilever. The extended monopole model used to model the magnetic tip sample interactions included two fitting parameters, q and δ. The values for q and δ were comparable to values found in the literature for similar DC-MFM current sensing experiments [38] [6]. However, the values for q and δ that were needed to match experiment and theory for AC-MFM were surprisingly large, this difference needs to be further examined in order to understand the tip sample interaction when this technique is applied.

The DC-MFM noise floor appears from the inability of our electronic measurement apparatus to detect phase changes smaller than 0.2 degrees. In contrast, the AC-MFM technique noise floor is consistent with the amplitude noise caused by mechanical thermal noise fluctuations at room temperature [61]. In order to measure viscous electron flow in a 2DEG, currents under the microampere range need to be measured. In the next Chapter, ideas to improve MFM current sensing will be discussed. However, the substantial gain in AC current sensitivity is important because it opens the possibility of studying electromigration in new materials and lower current densities. Also, since AC-MFM is able to detect currents several microns away from the tip [78], it could b e used for current detection in wires buried deep under other materials.

Chapter 4

Summary and Future Work

4.1 Hot electron transport

The effect of hot electrons on momentum scattering rates in a 2DEG was critically examined. It was shown that with hot electrons it is possible to explore the temperature dependence of individual scattering mechanisms not easily probed under equilibrium conditions. Namely, we were able to discern the Bloch-Grüneisen (BG) phonon scattering phenomena and the reduction in impurity scattering, both of which are not easy to detect under equilibrium conditions. The ETM model's prediction is consistent with the results obtained from hot electrons experiments. As a function of bias current, a resistance peak is formed in a 2DEG if the low temperature impurity limited mobilities $\mu_I(T = 0)$ is comparable to $\mu_{ph}(T_{BG})$ the phonon limited mobility at the critical BG temperature. In this case, as the bias current is increased, the electron temperature T_e rises due to Joule heating and the rapid increase in phonon scattering can be detected before the effect of the reduction in impurity scattering sets in. If $\mu_I(T = 0) \ll \mu_{ph}(T_{BG})$, there is no peak in resistance because the impurity scattering dominates sufficiently and its reduction has a much stronger effect on the total resistance than the rise in phonon scattering.

In order to further strengthen our theoretical explanation, we need to conduct experiments with higher mobility samples to ensure that the results of de Jong *et al.* [20] are not specific to their sample. Also T_e needs to be measured so that the need to calculate the energy relaxation rate is eliminated. This can be achieved by using a quantum point contact (QPC) as a thermometer, which would work up to a few Kelvin [4], or an electrical Johnson noise measurement, which would be difficult below a few Kelvin but would work up to arbitrarily high temperatures [39].

The ETM model fails at high fields because of non-linear phonon scattering effects and significant deviations of the electronic distribution away from the equilibrium Fermi distribution function f. The Green's function based theory of Lie *et al.* [41], which has been verified at high fields [31], needs to be compared to the results presented in this thesis using the ETM model for low to moderate fields. If impurity scattering can be reduced even further, and 2DEGs with mobilities of 100 $\times$ 10^6 cm^2/Vs realized, then the BG effect would be detectable even in equilibrium measurements.

4.2 Viscous electronic flow

In hot electrons, as T_e rises, l_{ee} falls and can be made much smaller than the momentum scattering length l_m and the characteristic size of a device W. If the boundaries of such a a device are rough, then a small l_{ee} could induce momentum transfer from the electrons to the boundaries and this "viscous effect" would influence the velocity profile of electronic flow. The existence of electron gas viscosity relies on the efficiency of electron-electron (e-e) scattering. In Reference [27], it is argued that e-e scattering is largely small angle in a 2DEG. In which case our estimate of l_{ee} is smaller than the true momentum diffusion length and we have overestimated the role of viscosity. So far studies of energy dependent e-e scattering have been conducted for electrons injected through a quantum point contact [42] [54]. More theory and experiments are required to gain a deeper understanding of the nature of the e-e scattering process with respect to momentum diffusion.

Assuming that Equation (2.14) is the momentum scattering rate for electrons,

Reference [20] predicts Poiseuille flow for ≈ 10 μA of current flowing through a wire of width $W > 5$ μm defined in a high mobility 2DEG with rough boundaries. The rough boundaries can be realized by defining the wire with a focused ion beam (FIB) tool rather than Schottky gates [70]. A current of ≈ 10 μA would produce a magnetic field of ≈ 10 μT around the wire and an appropriate microscopic magnetic sensing probe could image Poiseuille flow if it exists.

The transition from Knudsen (Ballistic) to Poiseuille flow has been studied extensively for classical gases, both experimentally [37] and analytically [18]. Also, direct simulation Monte Carlo (DSMC) methods made popular by G. A. Bird [12] have been able to successfully simulate this transition. The DSMC method involves tracking the trajectory of a small number of "representative" particles within "cells". Each "representative" particle represents a large number of real particles of a system and thereby a significant economy in computation is achieved. In simulating a classical gas, the trajectory of the particles are calculated in time steps that are roughly equal to the particle-particle scattering time. Further, collisions between particles of neighboring cells are taken into account using statistics arising from kinetic theory [24]. In DSMC, long range interactions are hard to incorporate [12]. If for a 2DEG, the screening is strong enough to limit long range interactions, and the mechanics of e-e scattering are better understood, it could be useful to attempt DSMC simulations of 2DEG flow. Such a simulation would give us a more precise knowledge of the conditions needed to see fluid-like behavior. Experimentally though, the ultimate proof of fluid-like behavior in electron flow would be in imaging it.

4.3 Current imaging

The possibility of imaging Poiseuille flow using MFM was explored since it had already been demonstrated to image magnetic media in the sub-100 nm range [9]. The experiments with imaging periodic nanomagnetic arrays allowed us to verify the possible sub-100 nm spatial resolution performance of MFM and also measure the magnetic field emanating from the tip. When MFM was deployed to sense DC currents (DC-MFM), only large currents greater than $\approx$ 2mA could be detected. To improve the current sensitivity, alternating currents at the resonant frequency of the cantilever were used (AC-MFM). This technique exploited the mechanical gain of the system and improved the current sensing ability by two orders of magnitude to $\approx$ 20 μA. However, this large increase in current sensitivity was accompanied by a substantial drop in the spatial resolution from sub-micron to several microns. This loss in spatial resolution is not currently understood. The large effective lift height that is required in the extended magnetic monopole model to simulate the magnetic interaction between an AC current carrying wire and the tip implies that a much larger volume of the tip interacts with a magnetic field produced by an AC current as compared to DC current. A more complete theory that explains this difference in interaction needs to be constructed.

The magnetic field produced by a current must interact with a smaller portion of the magnetic tip to improve spatial resolution. This could be achieved by depositing magnetic material only at the very end of the tip [14] rather than sputtering a magnetic thin film over the entire tip. The reduction in magnetic material would surely reduce the magnetic interaction force and hence reduce the sensitivity of MFM

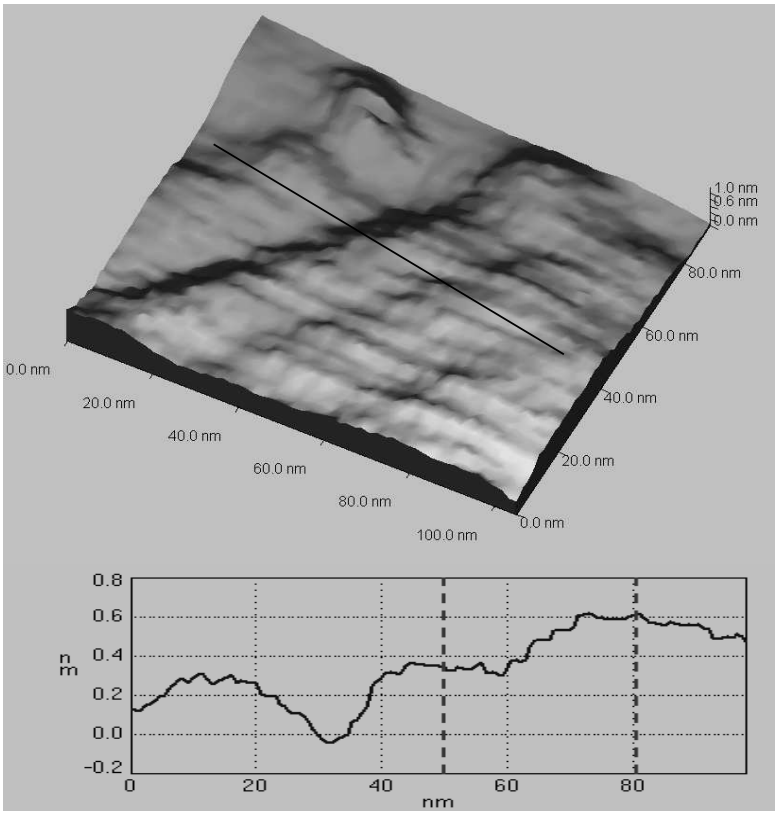

Figure 4.1: Non-Contact cryogenic AFM scan of Au on mica. The monoatomic steps of 0.27nm can be seen in the line profile. This scan was 105 nm x 90 nm in area and was taken at 5 K.

to magnetic fields. However, the MFM signal strength is proportional to $Q^{1/2}$ [63] and by operating in vacuum, it is known that the Q of the cantilever can improve by three orders of magnitude [2]. Therefore, it should be possible to increase the signal strength by a factor of thirty. Also, the noise floor which arises from the thermally induced fluctuations of the cantilever can be reduced by working at cryogenic temperatures.

The preliminary effort to realize a high vacuum cryogenic MFM is in progress.

A non-contact AFM image of gold atomic steps is shown in Figure 4.1. This image was taken using an Omicron SPM which has an interferometric cantilever deflection measurement system. The interferometric sensor requires a single-mode fiber to be aligned in close proximity to the cantilever probe through a temperature range of 5-300 K. Since there are no means to re-align the fiber and the tip once the SPM is placed the vacuum chamber, small thermal drifts that cause the interferometric system to fail at low temperatures were not correctable. At first, the reliability of the alignment was improved by switching the adhesive that was used to secure the fibre from the original UV cured Norland 8101 optical adhesive to a Henkel epoxy. However, the long term stability of the alignment is still poor.

The interferometric detection system relies on a laser which could cause heating of the device being imaged. To improve the reliability of the SPM and also make it more versatile, we are considering switching to a piezoresistive deflection measurement system. This change would eliminate the alignment problems of the interferometric system. Since there are eight spare electrical leads that reach the head of the microscope, biasing a piezoresistive cantilever should be feasible. If piezoresistive cantilevers are successfully deployed, the full multi-mode cantilever dynamical model developed by M. H. Wang [78] could be used to quantitatively model the the higher sensitivity of low temperature piezoresitve SPMs operated at higher order flexural modes [75]. In addition, Vodolin *et al.* [75] state that this higher sensitivity allows a reduction in power supplied to the piezoresitive cantilever, a feature that could be significant when attempting to maintain low sample temperatures.

4.4 Closing remarks

This thesis has attempted to further our understanding of electron transport by applying the ETM model to determine the role of various scattering mechanisms. This model was then compared to experimental measurements. Concurrently, a method to use MFM as a tool to sense electron flow was developed. The theory and experiments were designed with the hope of understanding under what conditions viscous effects could appear in a 2DEG, and assuming that viscous effects actually exist, developing the appropriate imaging technique to detect them.

Viscous effects, in the simplest sense of momentum diffusion, must exist in a 2DEG because e-e scattering does occur. However, the significance of viscosity on electron transport is yet to be conclusively determined. Experiments and theory that attempt to explore the effects of electron viscosity would further our intuition and understanding of electron transport.

Appendix A

Device Fabrication and Cryogenic Electrical Measurement

A.1 Device fabrication

The fabrication of the device involved three steps:

- Defining a mesa to isolate a region of the chip.
- Making Ohmic contacts to the 2DEG.
- Making Schottky gates to define the device.

Mesa etch

The wafer was first cleaned with acetone, methanol and ethanol and then baked (to evaporate the solvents) for 30 minutes at 200 ∘C. After which an optical lithography step using photoresist AZ-4620 was used to define regions of the wafer that had to be protected from the mesa-defining wet-etch. The exposure time was 1 minute, and

after developing with AZ-440-MIF for 40 seconds, the chip was hard-baked at 180 °C for 25 minutes.

The mesa was defined using a H_2SO_4:H_2O_2:H_2O (1:8:1000) solution. The etch rate had to be calibrated on every occasion because it was very sensitive to temperature. A typical etch rate was approximately 30 nm/min.

Ohmic Contacts

Another optical lithography step is used to define the regions where the Ohmic contact metals need to be deposited. This was done using AZ-5214 resist in "image-reversal" mode and developed with AZ-422-MIF. The chip was then briefly dipped into a solution of NH_4OH:H_20 (1:20) for 10 seconds and then blown dry using N_2 before quickly placing the chip into the electron beam metal evaporator.

The metals that were deposited were in the sequence Ni:Au:Ge:Au:Ni:Au with thicknesses 5 nm:5 nm:25 nm:10 nm:10 nm: 60 nm respectively (the first Ni surface being the one to be first deposited on the wafer) [1]. After metal deposition was complete, the "lift-off" process was completed by dipping the wafer in acetone for a few minutes and then rinsing it with ethanol.

In order to anneal the Ohmic contacts, the chip was rapid thermal annealed (RTA). The RTA sequence involved using an RTA oven which first raised the sample temperature in the following sequence: 110 °C for 60s, 260 °C for 20s, and 410 °C for 40s. All ramps in temperature were done at the rate of 30 °C/s.

Schottky gates

[1] Ohmic contact metal layers suggested by Mark Topinka.

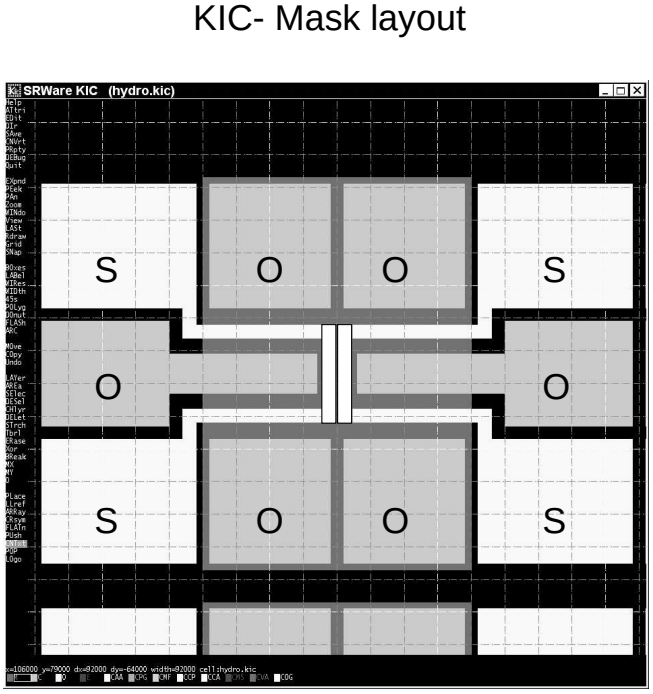

Figure A.1: The free software, KIC, was used to do mask layout. A screen capture of the mask layout program is shown. The dark grey region is the mesa mask, the light grey the Ohmic contact mask (labeled 'O'), and the white portions is the Schottky gate mask (marked 's'). If the bond pads are made > 100 μm $\times$ 100 μm it makes it easy to wire bond. It is convenient to allow for errors of +/- 10 μm in the alignment between masks.

The last optical lithography step is used to define the regions where the Schottky contact metals need to be deposited. This was done also with AZ-5214 resist in "image-reversal" mode. The resist had to be exposed for 3 seconds, then soft-baked for 52seconds on a hot-plate at 105 C and then flood-exposed for up to 2 minutes. The bilayer of 25 nm Ni and 150 nm Au was deposited and a similar "lift-off" process was followed as in the case of Ohmic contacts (and no RTA). The thickness of the

metal layers should be made greater than 100 nm to ensure that wire-bonding to the layers is easy.

A.2 Cryogenic electrical measurement

The devices were tested in Desert Cryogenics probe station model FS-Prober System. This cryogenic probe station is able to cool down samples to 1.5 K. The the chip was first soldered onto an all-metallic gold plated chip carrier (Spectrum Materials part no. HYB03401) using Indium foil (Lakeshore part no. IF-5). The chip carrier was then soldered onto a oxygen free high conductivity (OFHC) copper plate using Indium foil solder. The soldering was done by placing a sheet of Indium foil between the chip and the chip-carrier, and the chip-carrier and the copper plate and heating all three above 430 K (the melting point of Indium) using a hot plate. The copper plate was then screwed onto the cold finger of the cryostat. The copper plate surface which was in contact with the cold finger was polished and electroplated with gold to ensure a good thermal contact. A temperature sensor attached to the chip carrier recorded 2 K when the cold finger measured 1.5 K; this could have been caused because the Indium foil thermal conductivity falls below its superconducting transition of 3.37 K. It was found that 'GE' varnish and Apezon-N grease were not good substitutes for Indium foil as cryogenic adhesives for the chip and chip-carrier. In using them, the lowest temperature attained on the chip carrier was 5 K.

In our experiments, the Schottky gates of our device were biased through the DC probe arms of the probe station and the Ohmic contacts were wire bonded using a gold wire bonder to the chip carrier leads. The chip carrier leads were biased through

DC wires that were installed on the cryostat. A set of 12 DC leads were introduced through one of the flanges made for the probe arms. A 19-pin vacuum feedthrough (Lakeshore part no. VFT19-F) was attached onto the flange and the internal wiring within the cryostat was done using a phosphor bronze (CuSnP alloy) twisted pair wire (Lakeshore part no. DT-32). This wire has a low thermal conductivity and is non-ferromagnetic. The twisted pair wire was wrapped a few times around the radiation shield and then several times around the stem of the cold finger and then glued in place using "GE" varnish ((Lakeshore part no. VGE-7031). Wrapping the wire around the radiation shield (temperature $\approx$ 14K) ensured that the cold finger was not significantly thermally loaded, and wrapping the wire around the cold finger itself ensured that the wires were at as low a temperature as possible.

The electrical measurements were made using an Agilent A4156 parameter analyzer. From the A4156, one signal module unit (SMU) was used to apply the bias to the Schottky gates of the device and another SMU was used to current bias and measure the voltage across the device in a four-point measurement scheme. The SMU was used in the 0 to 2.2V range with +/-2 μV resolution setting. Care must be taken to subtract the DC offset of the voltage measurement, which can be as high as 50 μV, so that no spurious divergence is measured in the resistance of the device at low currents when dividing the voltage reading by the current.

Appendix B

Transport Calculation details

B.1 Table of constants

Constant	Value
m_0	9.1×10^{-31} Kg
e	1.6×10^{-19} C
$\hbar$	$\frac{1}{2\pi} \times 6.63 \times 10^{-34}$ Js
k_B	1.39×10^{-23} J/K
ϵ_0	$8.85 \times 10_{-12}$ F/m
κ_0	12.91
m	$0.067m_0$
D	11.5 eV
h_{14}	1.2×10^9 V/m
s_l	5134 m/s
s_t	3004 m/s
ρ	5317 Kg/m^3

Table B.1: Values of universal constants and GaAs material pararmeters used in calculations.

B.2 Transport calculations

The theoretical formalism used in Chapter 2 is taken from References [56],[30], and [29]. Some of the details regarding the calculations from Chapter 2 are presented

below using the notation of Reference [30].

B.2.1 Wavefunction

Only intra-subband scattering within the lowest occupied subband of the QW is considered since for at low temperatures the second subband is not significantly populated.

The wavefunction of the first quantized state in terms of a 2D wave vector $\mathbf{k}$=($\mathbf{k_x}$,$\mathbf{k_y}$) along the heterointerface is given by

$$\psi(r,z) = \phi(z)exp(i\mathbf{k}\cdot\mathbf{r}) \tag{B.1}$$

where ϕ(z) denotes the quantized component of the wavefunction. We use the Fang-Howard variational approximation for ϕ(z) [67],

$$\phi(z) = (\frac{1}{2}b^3z^2)^{1/2}exp(-\frac{1}{2}bz) \tag{B.2}$$

with variational parameter b,

$$b = (\frac{12me^2}{\kappa_0\epsilon_0\hbar^2})^{1/3}(\frac{11}{32}n) \tag{B.3}$$

where m is the effective mass of the electron in GaAs, e is the magnitude of the charge of an electron, $\hbar$ the reduced Planck constant, ϵ the dielectric permittivity, κ_0 the static dielectric constant for GaAs, and n the concentration of the 2DEG.

B.2.2 Impurity scattering form factor

The for factor F in Equation (2.3) for impurity scattering is given by

$$F(q_{xy}, z) = \int dz |\phi(z)|^2 exp(-q_{xy}|z_i - z|) \tag{B.4}$$

Also, the impurity distribution $N(Z_I)$ in Equation (2.3) has two components: The remote ionized impurities and background impurities. The remote ionized impurities can be modeled as a plane of charged ions at a fixed distance d away from the 2DEG, and the background impurities modeled as a random distribution of charges throughout the entire heterostructure [19]. In our sample, it is the background remote ionized impurities that dominate [1]

The actual value of the background impurities is not known precisely and is the free parameter in our model. A value of $1.35\times10^15/\text{cm}^3$ was used to to model our sample and $0.75\times10^15/\text{cm}^3$ for de Jong *et al.* sample.

B.2.3 Phonon scattering matrix elements

The bare momentum scattering matrix elements in two dimensions $|C^p|^2$ included in Equation (2.4) are for deformation coupled (DP), longitudinal piezoelectric coupled (PE_l) and transverse piezoelectric coupled (PE_t) given by [57]:

$$|C_{DP}(q)|^2 = \frac{D^2 \hbar q}{2\rho u_l}, \tag{B.5}$$

$$|C_{DE_l}(q)|^2 = \frac{(eh_{14})^2 \hbar s_l}{2\rho s_l} \frac{9 q_z^2 q_{xy}^4}{2q(q_z^2 + q_{xy}^2)^3}, \tag{B.6}$$

[1] Private communication with A.C. Gossard (UCSB), whose research group grew the crystal sample. This result was confirmed by our calculations.

$$|C_{DE_t}(q)|^2 = \frac{(eh_{14})^2 \hbar s_t}{2\rho s_t} \frac{8q_z^4 q_{xy}^2 + q_{xy}^6}{4q(q_z^2 + q_{xy}^2)^3}, \tag{B.7}$$

where, D is the deformation potential constant, h_{14} is the piezoelectric constant, ρ is the density of GaAs, and s_l and s_t are the longitudinal and transverse sound velocities respectively in GaAs.

Also, the square of the Fourier transform of $\phi(z)$, represented as $|I(q_z)|^2$ in Equation (2.4), is given by [57],

$$|I(q_z)|^2 = \frac{b^6}{(b^2 + q_z^2)^3}. \tag{B.8}$$

B.2.4 Screening

The screening term $\epsilon(q_{xy}, T_e)$ is the same as that which is calculated in [67],

$$\epsilon(q_{xy}, T_e) = 1 + \frac{e^2 H(q_{xy}) \prod(q_{xy})}{2\epsilon_0 \kappa_0 q_{xy}} \tag{B.9}$$

where,

$$H(q_{xy}) = b(8b^2 + 9bq_{xy} + 3q_{xy}^2)/8(b + q_{xy})^3. \tag{B.10}$$

The temperature dependent static polarizability function $\Pi(q_{xy}, T_e)$ can be calculated using [46],

$$\Pi(q_{xy}, T_e, E_F) = \int_0^\infty \frac{\Pi(q_{xy}, 0, E'_F)}{4k_B T_e Cosh^2[(E_F - E'_F)/2k_B T_e]} dE'_F \tag{B.11}$$

with,

$$\Pi(q_{xy}, 0, E_F) = \frac{m}{\pi\hbar^2}(1 - \Theta(q_{xy} - 2k_F)(1 - (\frac{2k_F}{q_{xy}})^2)^{1/2}) \tag{B.12}$$

where, Θ is the unit step function and k_F is the Fermi wave vector.

B.3 Matlab code to calculate relaxation rates

transport.m Feb.18, 2004

```
% This routine calculates phonon momentum relaxation times
% by calling integrnd_lsp_mmm.m  (longitudinal phonon branch,
% piezo-electrically  coupled scattering rate)
% integrnd_tsp_mmm.m  (transverse  phonon branch,
% piezo-electrically  coupled scattering rate)
% integrnd_dps_mmm.m (longitudinal phonon branch,
% deformation coupled  scattering rate)
% Screening is included and temperature of the electrons and
% the phonons are kept track of independently Most of the theory
% of Hot electrons in GaAs/AlGaAs was done by P.J.Price.
% K.Hirakawa and H.Sakaki redo essentially the same theory
% and present the results more clearly in APL v49 p14 (1986) and
% PRB v33 p8291 (1986). Note that the PRB does not keep track
% of the fermi and bose statics carefully since it deals
% with mobility calculations in the equipartition regiem
% and not the Bloch-Gruneisen regime. The APL is more careful
% about this as it calculates the energy relaxtion rates.
% T. Kawamura and S. Das Sarma's PRB v45 p3612 is also a good
% reference to take a look at.

clear all
close all

warning off

global hbar n e m m0 kf vf Ef eV meV d dis h14 rho ul ut cl ...
                                ct k0 e0 b kB Sqt Q T TL TE B C Ct q
```

```
load SQT_2p0e15XX.mat;

n=2.0e15;              % density in /m^2
ti0=4.2e-10;  % impurity scattering time at T=0
Ni=6.1e15;             % concentration of the rempte ion impuritie
dis=400e-10;  % distance in meter of the remote ion impurities
nd=0;
e=1.6e-19;             % charge of electron
hbar = (1/((2*pi)))*6.63e-34; % Js
h  = hbar*2*pi;
m0 = 9.1e-31 ;
m  = 0.067*m0;
vf = (hbar/m)*(2*pi*n)^(1/2);
Ef = (1/2)*m*vf^2;
eV=e;
meV=0.001*eV;
d= 11.5*eV;
h14=1.2e+9;
cl=1.40e11;
ct=0.48e11;
rho=5317;
ul=sqrt(cl/rho);
ut=sqrt(ct/rho);
k0=12.91;
e0=8.85e-12;
b=(((12*m*e^2)/(k0*e0*hbar^2))*(nd+(11/32)*n))^(1/3);
kB=0.087*meV;
kf=sqrt(2*pi*n);
B=1/b;
C=hbar*ul/kB;
Ct=hbar*ut/kB;
fc=10;


Sqt=(1./Sqt).^2;
Sqt(1,:)=0;

min_ang=1e-3;
max_ang=pi;
min_qz=0;
max_qz=10*kf;
```

```
%min_E=0.001*Ef;
%max_E=5*Ef;


told=[0.1];
toll=[0.001];
tolt=[0.001];

Te=[1:0.2:2 2.5:0.5:5 6:1:20 40:20:100];  % electron T range

Tl=[1:1:10 12:2:20 40:20:80];                % lattice T range



inv_t_dp=zeros(size(Tl,2),size(Te,2));
inv_t_dps=zeros(size(Tl,2),size(Te,2));
inv_t_l=zeros(size(Tl,2),size(Te,2));
inv_t_t2=zeros(size(Tl,2),size(Te,2));   % Initializing arrays
inv_t_i=zeros(size(Tl,2),size(Te,2));
inv_t_si=zeros(size(Tl,2),size(Te,2));

r=0;
for TL=Tl;
   warning off
   r=r+1;
   c=0;
   res=[];

   for TE=Te;
         c=c+1;

        if TE>=TL   % no need to calculate TE<TL !

   tic
   max_E=Ef+fc*kB*TE;
   if fc*kB*TE<0.999*Ef
   min_E=Ef-fc*kB*TE;
   else
     min_E=0.001*Ef
     end
```

```
        warning off
    [n/1e15 TE TL]
result=4*trplquad('integrnd_dps_mmm',min_ang,max_ang,...
min_qz,max_qz,min_E,max_E,told,'quad8');
result_d=quad8('integrnd_mis_denom',0,max_E);

inv_t_dp(r,c)=[((m*(d^2)*((hbar*ul)))...
      /( 2*(2*pi)^2*(hbar^3)*cl))*...
result/(result_d))];

result=4*trplquad('integrnd_lsp_mmm',min_ang,max_ang,...
   min_qz,max_qz,min_E,max_E,toll,'quad8');
inv_t_l(r,c)=[((4.5*ul*m*(e*h14)^2)/( pi^2 * kB*TE*rho))...
      *(result/(result_d))];

result=4*trplquad('integrnd_tsp_mmm',min_ang,max_ang,...
   min_qz,max_qz,min_E,max_E,toll,'quad8');
inv_t_t(r,c)=[(((0.25)*m*ut*(e*h14)^2)/( pi^2 * kB*TE*rho ))...
      *(result/(1))];;

toc/60


        end

  end

end

inv_t_t=inv_t_t/2;

tdp=1./inv_t_dps;
tpl=1./inv_t_l;
tpt=1./inv_t_t;
ti=1./inv_t_i;
tsi=1./inv_t_si;

udp=(e/m)*tdp;
udp2=(e/m)*tdp2;
upl=(e/m)*tpl;
upt=(e/m)*tpt;
ui=(e/m)*ti;
```

```
usi=(e/m)*tsi;

uap=(1./udp + 1./upl + 1./upt).^-1;
uac=(1./udp + 1./upl + 1./upt + 1./ui).^-1;
uacs=(1./udp + 1./upl + 1./upt + 1./usi).^-1;


save molen2p2trans6_sub_delete

-------------------------------------------
integrnd_dps_mmm.m

function out = integrnd_dps_mmm(th,q,E)

global hbar n e m m0 kf vf Ef eV meV d rho ul ut cl ct k0 e0 b ...
   kB Sqt Q T TL TE B C Ct

k=sqrt(E.*(2*m/hbar^2));

out =(interp2(T,Q,Sqt,TE,2*k*abs(sin(th/2)),'nearest'))'.*. . .
(1-cos(th)).*...
1./(1-(1./(exp((1/(kB*TE)).*(E-Ef))+1))).*...
(1./((1 + (B^2 * q.^2)).^3) ).*...
sqrt((2.*k.*sin(th/2)).^2 + q.^2.).*...
(((1./(exp((C/TL).*(sqrt((2.*k.*sin(th/2)).^2 + q.^2)))-1)).*...
(1-(1./(exp((1/(kB*TE)).*(E-Ef+hbar*ul*sqrt((2.*k.*sin(th/2)).^2 ...
+ q.^2)))+1))))+...
(((1./(exp((C/TL).*(sqrt((2.*k.*sin(th/2)).^2 + q.^2)))-1))+1).*...
(1-(1./(exp((1/(kB*TE)).*(E-Ef-hbar*ul*sqrt((2.*k.*sin(th/2)).^2 + ...
q.^2)))+1)))).*st(E-hbar*ul*sqrt((2.*k.*sin(th/2)).^2 + q.^2))).*...
E.*(-1./(4*kB.*TE.*((cosh((1/(kB*TE)).*(E-Ef))).^2)));

-------------------------------------------

integrnd_lsp_mmm.m

function out = integrnd_lsp_mmm(th,q,E)

global hbar n e m m0 kf vf Ef eV meV d h14 rho ul ut cl ct k0 e0...
                    b kB Sqt Q T TL TE B C
```

```
k=sqrt(E.*(2*m/hbar^2));


out =(((q.^2).*((2.*kf.*sin(th/2)).^4 ))...
./((q.^2 + (2.*kf.*sin(th/2)).^2).^(3))).*...
(1./((1 + (B^2 * q.^2)).^3) ).*...
(((1./(exp((C/TL).*(sqrt((2.*kf.*sin(th/2)).^2 + q.^2)))-1)).*...
((1./(exp((C/TE).*(sqrt((2.*kf.*sin(th/2)).^2 + q.^2)))-1))+1))+...
((1./(exp((C/TE).*(sqrt((2.*kf.*sin(th/2)).^2 + q.^2)))-1)).*...
((1./(exp((C/TL).*(sqrt((2.*kf.*sin(th/2)).^2 + q.^2)))-1))+1))).*...
((1./(interp2(T,Q,Sqt,TE,2*kf*abs(sin(th/2))))).^2)';
```

---

integrnd_tsp_mmm

```
function out = integrnd_tsp_mmm(th,q)

global hbar n e m m0 kf vf Ef eV meV d h14 rho ul ut cl...
   ct k0 e0 b kB Sqt Q T TL TE B C Ct

K=1;

out =(( (8.*(q.^4).*((2.*kf.*sin(th/2).^2)))+(2.*kf.*sin(th/2)).^6 )...
   ./((q.^2 + (2.*kf.*sin(th/2)).^2).^3)).*...
    (1-cos(th)).*(1./((1 + (B^2 * q.^2)).^3) ).*...
    (((1./(exp((Ct/TL).*(sqrt((2.*kf.*sin(th/2)).^2 + q.^2)))-1)).*...
    ((1./(exp((Ct/TE).*(sqrt((2.*kf.*sin(th/2)).^2 + q.^2)))-1))+1))+...
    ((1./(exp((Ct/TE).*(sqrt((2.*kf.*sin(th/2)).^2 + q.^2)))-1)).*...
    ((1./(exp((Ct/TL).*(sqrt((2.*kf.*sin(th/2)).^2 + q.^2)))-1))+1))...
    .*(1./(interp2(T,Q,Sqt,TE,2*kf*abs(sin(th/2))))).^2)';
```

Integrnd_si_ppE

```
function out = integrnd_si_ppE(th,E)

global hbar n e m m0 kf vf Ef eV meV dis d rho ul ut ...
   cl ct k0 e0 b kB Sqt Q T TL TE B C Ct

k=sqrt((2*m*E)/(hbar)^2);


out =(1/2)*(((interp2(T,Q,Sqt,TE,2*k.*abs(sin(th/2))))))'.*. . .
   (1-cos(th)).*...
   ((b./(b + 2.*k.*sin(th/2))).^6).*...
   (((exp(-2.*k.*sin(th/2)*dis))./(2.*k.*sin(th/2))).^2).*...
   (1-(1./(exp((1/(kB*TE)).*(E-Ef))+1)));
```

Screenig **function** table generator ....

runscreen.m

```
global hbar n e m m0 kf vf Ef eV meV d h14 rho ul ut ...
   cl ct k0 e0 b kB TL TE B C Ct

T1=[1:0.1:5];
T2=[6:1:100];
T=[T1,T2];

n=2.2e15;              % density in /m^2
ti0=6.2e-11;  % impurity scattering time at T=0
nd=0;
e=1.6e-19;             % charge of electron
hbar = (1/((2*pi)))*6.63e-34;
h= hbar*2*pi;
m0 = 9.1e-31 ;
m  = 0.067*m0;
vf = (hbar/m)*(2*pi*n)^(1/2);
Ef = (1/2)*m*vf^2;
eV=e;
meV=0.001*eV;
d= 11.5*eV;
h14=1.2e+9;
ul=473;
ut=334;
```

```
cl=1.40e11;
ct=0.48e11;
rho=5317;
ul=sqrt(cl/rho);
ut=sqrt(ct/rho);
k0=12.91;                                                    290
e0=8.85e-12;
b=(((12*m*e^2)/(k0*e0*hbar^2))*(nd+(11/32)*n))^(1/3);

kB=0.087*meV;
kf=sqrt(2*pi*n);
B=kf/b;
C=hbar*ul*kf/kB;
Ct=hbar*ut*kf/kB;


                                                             300
Q=[0:0.00001*kf:0.00005*kf, 0.1*kf:0.05*kf:1.8*kf,...
      1.81*kf:0.01*kf:2.2*kf,2.25*kf:0.05*kf:2.6*kf,...
      2.8*kf:0.1*kf:3*kf, 3.2*kf:0.2*kf:16*kf];



Sqt=zeros(size(Q,2),size(T,2));

      for ctr=1:size(T,2)
      n                                                      310
      tic
        for cqr=1:size(Q,2)
        Sqt(cqr,ctr)=S(Q(cqr),T(ctr));
        end
      tim=toc;
      approx_time_left=(size(T,2)-ctr)*tim/60
   end

save('SQT_2p2e15XX','Sqt','Q','T')
                                                             320
-------------------------------------

function out = S(q,T)

global hbar n e m m0 kf vf Ef eV meV d rho ul ut cl...
   ct k0 e0 b kB TL B C Ct
```

```
out=1+((e^2)./(2*k0*e0.*q)).*pol(q,T).*...
   ((b*(8*b^2+9*b.*q+3.*(q.^2))).(8.*((b+q).^3)));
```

330

```
--------------------------------------
function out = pol(q,T)

global hbar n e m m0 kf vf Ef eV meV d rho ul ut cl..
ct k0 e0 b kB TL B C Ct


out=quad8('int_pol',0.0001*Ef,4*Ef,[0.0001],[],q,T);

--------------------------------------                    340


function out = int_pol(Efp,q,T)

global hbar n e m m0 kf vf Ef eV meV d rho ul ut cl...
   ct k0 e0 b kB TL TE B C Ct


kfp=sqrt((2*m/((hbar)^2)).*Efp);
out=(m/(pi*(hbar^2)*4*kB*T)).*(1-st(q-2.*kfp).*...                350
   (abs(sqrt((1-(2.*kfp./q).^2)))./...
   ((  cosh(((Ef  -  Efp)./(2*kB*T))).^2));


--------------------------------------
```

Bibliography

[1] M. C. Abraham, H. Schmidt, T. A. Savas, Henry I. Smith, R. J. Ram, and C. A. Ross. Magnetic properties and inteactions of single-domain nanomagnets in a period array. *J. Appl. Phys.*, 89:5667, 2001.

[2] T. R. Albrecht, P. Grtter, D. Horne, and D. Rugar. Frequency modulation detection using high-q cantilevers for enhanced microscope sensitivity. *J. Appl. Phys.*, 69:668, 1991.

[3] T. Ando, A.B. Fowler, and F. Stern. Electronic properties of two-dimensional systems. *Rev. Mod. Phys.*, 54:437, 1982.

[4] N. J. Appleyard, J. T. Nicholls, M. Y. Simmons, W. R. Tribe, and M. Pepper. Thermometer for the 2d electron gas using 1d thermopower. *Phys. Rev. Lett.*, 81:3491, 1998.

[5] N. W. Ashcroft and N. D. Mermin. *Solid State Physics*. Saunders College Publishing, Orlando, Florida, USA, third edition, 1976.

[6] K. L. Babcock, V. B. Elings, J. Shi, D. D. Awschalom, and M. Dugas. Field-dependence of microscopic probes in magnetic force microscopy. *Appl. Phys. Lett.*, 69(5):705–707, July 1996.

[7] C. W. J. Beenakker. Random-matrix theory of quantum transport. *Rev. Mod. Phys.*, 69:731, 1997.

[8] L. Belliard, A. Thiaville, S. Lemerle, A. Lagrange, J. Ferre, and J. Miltat. Investigation of the domain contrast in magnetic force microscopy. *J. Appl. Phys.*, 81(8):3849–3851, April 1997.

[9] S. J. Bending. Local magnetic probes in supercondcutors. *Advances in Physics*, 48(4):449–535, July 1996.

[10] G. Binning, C. F. Quate, and C. Gerber. Atomic force microscope. *Phys. Rev. Lett.*, 56(9):930–933, March 1986.

[11] G. Binning, H. Rohrer, C. Gerber, and E. Yeibel. Tunneling through a controlable vacuum gap. *Appl. Phys. Lett.*, 40:178, 1982.

[12] G. A. Bird. *Molecular gas dynamics and the simulation of gas flows*. Oxford University Press, New York, New York (USA), second edition, 1994.

[13] V. Chabasseur-Molyneux, A. S. Dzurak, A. Kozorezov, J. K. Wigmore, D. A. Ritchie, A. C. Churchill, and M. Pepper. Observation of the effect of electron-electron scattering on the impurity limited resistivity of a two-dimensional electron gas. *Phys. Rev. B*, 51(19):13793, 1995.

[14] A. R. Champagne, A. J. Couture, F. Kuemmeth, and D. C. Ralph. Nanometer-scale scanning sensors fabricated using stencil lithography. *Appl. Phys. Lett.*, 82(7):1111–1113, February 2003.

[15] A. M. Chang, H. D. Hallen, L. Harriott, H. F. Hess, H. L. Kao, J. Kwo, R. E. Miller, R. Wolfe, J. van der Ziel, and T. Y. Chang. Scanning hall probe microscopy. *Appl. Phys. Lett.*, 61(16):1974, 1992.

[16] A. V. Chaplik. Energy spectrum and electron scattering in inversion layers. *Zhurnal Eksperimental'noi i Teoreticheskoi Fiziki*, 60:1845, 1971.

[17] A. R. Choudhuri. *The physics of fluids and plasmas*. Cambridge University Press, Cambridge, UK, first edition, 1998.

[18] R. Datta and R. G. Rinker. Tubes of circular cross-section. *The Cannadian Journal of Chemical Engineering*, 59:268, 1981.

[19] J.H. Davies. *The physics of low-dimensional semiconductors*. Cambridge University Press, Cambridge, UK, first edition, 1998.

[20] M. J. M. de Jong and L. W. Molenkamp. Hydrodynamic electron flow on high-mobility wires. *Phys. Rev. B*, 51(19):13389, 1995.

[21] C. W. de Silva. *Vibration: Fundamentals and Practice*. CRC Press, New York, New York, first edition, 2000.

[22] H. Ehrenreich and D. Turnbull (eds.). *Solid State Physics: Semiconductor Heterostructures and Nanostructures*. Springer-Verlag, San Diego, California , USA, third edition, 1991.

[23] M. A. Eriksson, R. G. Beck, M. Topinka, J. A. Katine, R. M. Westervelt, K. L. Campman, and A. C. Gossard. Cryogenic scanning probe characterization of semiconductor nanostructures. *Appl. Phys. Lett.*, 69:671, 1996.

[24] A. L. Garcia. *Numerical methods for Physics*. Prentice Hall, Upper Saddle River, New Jersey (USA), second edition, 2000.

[25] G.F. Giuliani and J.J. Quinn. Lifetime of a quasiparticle in a two-dimensional electron gas. *Phys. Rev. B*, 26:4421, 1982.

[26] R. N. Gurzhi. Minimum of resistance in impurity free conductors. *Journal of Experimental and Theoretical Physics (U.S.S.R.)*, 44:771, 1963.

[27] R. N. Gurzhi, A. N. Kalinenko, and A. I. Kopeliovich. Electron-electron collisions and a new hydrodynamic effect in two-dimensional electron gas. *Phys. Rev. Lett.*, 74:3872, 1995.

[28] U. Hartmann. The point dipole approximation in magnetic force microscopy. *Phys. Lett. A: Mater. Sci. Process*, 137(9):475–478, June 1989.

[29] K. Hirakawa and H. Sakaki. Energy relaxation of two-dimensional electrons and the deformation potential constant in selectively doped algaas/gaas heterojunctions. *Appl. Phys. Lett.*, 49(14):889, 1986.

[30] K. Hirakawa and H. Sakaki. Mobilitiy of the two-dimensional electron gas at selectively doped n-type algaas/gaas with controlled electron concentrations. *Phys. Rev. B*, 33:8291, 1986.

[31] K. Hirakawa and H. Sakaki. Hot-electron transport in selectively doped algaas/gaas heterojunctions. *J. Appl. Phys.*, 63(3):803, 1988.

[32] H. J. Hug, B. Stiefel, P. J. A. van Schendel, A. Moser, R. Hofer, S. Martin, H. J. Guntherodt, S. Porthun, L. Abelmann, J. C. Lodder, G. Bochi, and R. C. O'Handley. Quantitative magnetic force microscopy on perpendicularly magnetized samples. *J. Appl. Phys*, 83(11):5609–5620, June 1998.

[33] M. Hwang, M. C. Abraham, T. A. Savas, Henry I. Smith, R. J. Ram, and C. A. Ross. Magnetic force microscopy study of inteactions in 100nm period nanomagnet arrays. *J. Appl. Phys.*, 87:5108, 2000.

[34] M. Jang, Y. Kim, J. Shin, S. Lee, and K. Park. A 50-nm-gate-length erbium-silicided n-type schottky barrier metal-oside-semiconductor field-effect transistor. *Appl. Phys. Lett.*, 84:741–743, February 2004.

[35] T. Kawamura and S. Das Sarma. Phonon scattering limited electron mobilities in algaas/gaas heterojunctions. *Phys. Rev. B*, 45:3612, 1992.

[36] J. R. Kirtley and J. P. Wikswo Jr. Scanning squid microscopy. *Annu. Rev. Mater. Sci.*, 29:117–148, 1999.

[37] M. Knudsen. Die gesetze der molecular stromung und dieinneren reibungstromung der gase durch rohren. *Ann. Phys.*, 28:75, 1909.

[38] L. Kong and S. Y. Chou. Quantification of magnetic force microscopy using a micronscale current ring. *Appl. Phys. Lett.*, 70(15):2043–2045, April 1997.

[39] C. Kurdak, D. C. Tsui, S. Parihar, S. A. Lyon, and M. Shayegan. Elctron temperature in low-dimensional wires using thermal noise measurements. *Appl. Phys. Lett.*, 67:386, 1995.

[40] X. L. Lei, J. L. Birman, and C. S. Ting. Two-dimensional balance equations in nonlinear electronic tranport and application to gaas-gaalas heterojunctions. *J. Appl. Phys.*, 58:2270, 1985.

[41] X. L. Lei and C. S. Ting. Green's-function approach to nonlinear electronic transport for an electron-impurity-phonon system in a strong electric field. *Phys. Rev. B*, 32:1112, 1985.

[42] B.J. LeRoy, A. C. Bleszynski, M.A. Topinka, R. M. Westervelt, S.E.J. Shaw, E.J. Heller, K.D. Maranowski, and A.C. Gossard. Imaging coherent electron flow. *Physics of Semiconductors*, 171:169, 2002.

[43] E. M. Lifshitz and L. P. Pitaevskii. *Physical Kinetics, Landau and Lifshitz Course of theoretical Physics Volume 10.* 1980.

[44] J. Lohau, S. Kirsch, A. Carl, G. Dumpich, and E. F. Wassermann. Quantitative determination of effective dipole and monopole moments of magnetic force microscopy tips. *J. Appl. Phys.*, 86(6):3410–3417, 1999.

[45] M. Lundstrom. *Fundamentals of carrier transport.* Cambridge University Press, Cambridge, UK, second edition, 2000.

[46] P. F. Maldague. Many-body corrections to the polarizability of the two-dimensional electron gas. *Surface Science*, 73:296, 1978.

[47] H. J. Mamin, D. Rugar, J. E. Stern, B. D. Teris, and S. E. Lambert. Force microscopy of magnetization patterns in longitudinal recording media. *Appl. Phys. Lett*, 53:1563, 1988.

[48] Y. Martin and H. K. Wickramasinghe. Magnetic imaging by "force microscopy" with 1000 angstrom resolution. *Appl. Phys. Lett*, 50:1455–1457, 1987.

[49] S. McVitie, R. P. Ferrier, J. Scott, G. S. White, and A. Gallagher. Quantitative field measurements from magnetic force microscope tips and comparison with point and extended charge models. *J. Appl. Phys.*, 89(7):3656–3661, April 2001.

[50] J. M. Papria and T. L. Rhodes. First observation of knudsen minimum in normal liquid ^{3}he. *Phys. Rev. Lett.*, 51:805, 1983.

[51] L. Pfeiffer, K.W. West, H.L. Stromer, and K.W. Baldwin. Electron mobilities exceeding 10^7 cm^2/vs in modulation doped gaas. *Appl. Phys. Lett.*, 55:1880–90, 1989.

[52] G. N. Phillips, M. Seikman, L. Abelmann, and J. C. Lodder. High resolution magnetic force microscopy using focused ion beam modified tips. *Appl. Phys. Lett.*, 81(5):865–867, February 2002.

[53] S. Porthun, L. Abelmann, and C. Lodder. Magnetic force microscopy of thin film media for high density magnetic recording. *Journal of Magnetism and Magnetic Materials*, 182(1-2):238–273, feb 1998.

[54] H. Predel, H. Buhmann, L. W. Molenkamp, R. N. Gurzhi, A. N. Kalinenko, and A. I. Kopeliovich. Effects of electrons-electrons scattering on electron-beam propagation in a two dimensional electron gas. *Phys. Rev. B*, 62:2057, 2000.

[55] P. J. Price. Hot electrons in a gaas heterolayer at low temperature. *J. Appl. Phys.*, 53:6863, 1982.

[56] P. J. Price. Heterolayer mobility in the bloch-grüneisen range. *Solid State Communications*, 51(8):607, 1984.

[57] P. J. Price. Low temperature two-dimensional mobility of a gaas heterolayer. *Surface Science*, 143:145, 1984.

[58] U. Rabe and W. Arnold. Need title. *Ann. Phys.*, 3:589, 1994.

[59] U. Rabe, K. Janser, and W. Arnold. Vibrations of free and surface-coupled atomic force microscope cantilevers: Theory and experiment. *Rev. Sci. Instrum.*, 67(9):3281–3293, September 1996.

[60] D. Rugar, H. J. Mamin, P. Guethner, S. E. Lambert, J. E. stern, I McFadyen, and T. Yogi. Magnetic force microscopy: General principles and application to longitudinal recording media. *J. Appl. Phys.*, 68:1169–1183?, 1990.

[61] M. V. Salapaka, H. S. Bergh, J. Lai, A. Majumdar, and E. McFarland. Multi-mode nosie analysis of canitlevers for scanning probe microscopy. *J. Appl. Phys.*, 81:2480, 1997.

[62] A. Sandhu, H. Masuda, A. Oral, S. J. Bending, A Yamada, and M. Konagai. Room temperature scaning hall probe microscopy using gaas/algaas and bi micro-hall probes. *Ultramicroscopy*, 91(1-4):97–101, November 2002.

[63] D. Sarid. *Scanning Force Microscopy.* Oxford University Press, Oxford, UK, second edition, 1994.

[64] T. A. Savas, M. Farhoud, Henry I. Smith, M. Hwang, and C. A. Ross. Properties of large-area nanomagnet arrays with 100 nm period made by interferometric lithography. *J. Appl. Phys.*, 85:6560, 1999.

[65] J. Scott, S. McVitie, R. P. Ferrier, and A. Gallagagr. Electrostatic charging artefacts in lorents electron tomography of mfm tip stray fields. *Journal of Physics D: Applied Physics*, 34:1326, 2001.

[66] George D. Skidmore and E. Dan Dahlberg. Improved spatial resolution in magnetic force microscopy. *Appl. Phys. Lett.*, 71(22):3293–3295, December 1997.

[67] F. Stern. Self-consistent results for n-type si inversion layers. *Phys. Rev. B*, 5:4891, 1972.

[68] H. L. Stormer, L. N. Pfeiffer, K. W. Baldwin, and K. W. West. Observation of a bloch-grneisen regime in two-dimensional electron transport. *Phys. Rev. B*, 41:1278, 1990.

[69] H.L. Stormer, D. C. Tsui, and A. C. Gossard. The fractional quantum hall effect. *Rev. Mod. Phys.*, 71:S298, 1999.

[70] T. J. Thornton, M. L. Roukes, A. Scherer, and B. P. Van de Gaag. Boundary scattering in quantum wires. *Phys. Rev. Lett.*, 63:2128, 1989.

[71] M.A. Topinka, B.J. LeRoy, S.E.J. Shaw, E.J. Heller, R. M. Westervelt, K.D. Maranowski, and A.C. Gossard. Imaging coherent electron flow from a point contact. *Science*, 289:2323, September 2000.

[72] H. van Houten, B. J. van Wees, J.E. Mooij, C.W. J. Beenakker, J.G. Williamson, and C.T. Foxon. Coherent electron focusing in a two-dimensional electron gas. *Europhysics Letters*, 5:721, 1988.

[73] P. J. van Schendel, H. J. Hug, B. Stiefel, S. Martin, and H.-J. Guntherodt. A method for the calibration of magnetic force microscopy tips. *J. Appl. Phys*, 88(1):435–445, July 2000.

[74] C. Veauvy, K. Hasselbach, and D. Mailly. Scanning μ-superconducting quantum interference device force microscopy. *Rev. Sci. Instrum.*, 73(11):3825–3830, 2002.

[75] A. Volodin and C. Van Haesendonck. Low temperature force microscopy based on piezoresistive cantilevers operating at a higher flexural mode. *Applied Physics A: Materials Science and Processing*, 66, 1998.

[76] L. N. Vu and D. J. Van Harlingen. Design and implementation of a scanning squid microscope. *IEEE Trans. Appl. Superd.*, 3(1):1918–1921, March 1993.

[77] W. Walukiewicz, H.E. Ruda, J. Lagowski, and H.C. Gatos. Electron mobilities in modulation-doped heterostructures. *Phys. Rev. B*, 30:4571, 1984.

[78] M. H. Wang. *Study of current measurement in magnetic force microscopy.* Master of electrical engineering and computer science thesis, Massachusetts Institute of Technology, 2001.

[79] W. T. Wilson, Johnny K. O. Sin, and S. Simon Wong. A novel crosstalk isolation structure for bulk cmos power ic's. *IEEE. Trans. Electron. Devices*, 45(7):1580–1586, July 1998.

[80] R. Yongsunthon, J. McCoy, and E. D. Willianms. Evaluation of mfm for probing electromigration processes. *Characterization and metrology for ULSI technology - AIP Conference Proceedings*, (550):630–634, 2001. Editors: D. G. Seiler and A. C. Diebold and T. J. Shaffner and R. McDonald and W. M. Bullis and P. J. Smith and E. M. Secula.

[81] R. Yongsunthon, A. Stanishevsky, J. McCoy, and E. D. Willianms. Observation of current crowding near fabricated voids in gold lines. *Appl. Phys. Lett.*, 78(18):2661–2663, 2001.

[82] P. Y. Yu and M. Cardona. *Fundamentals of Semiconductors: Physical and Material Properties.* Academic Press Inc., San Diego, California , USA, second edition, 2001.

[83] Z. Z. Yu, M. Haerle, J. W. Zwart, J. Bass, W. P. Pratt Jr., and P. A. Schroeder. Negative temperature derivative of resistivity in thin potassium samples: The gurzhi effect? *Phys. Rev. Lett.*, 52:368, 1984.

[84] J. Zhao, W. P. Pratt, Jr., H. Sato, P. A. Schroeder, and J. Bass. Electronic transport properties of thin potassium wires below 1 k. i. derivative of electrical resistivity. *Phys. Rev. B*, 37:8738, 1988.

[85] J. M. Ziman. *Principles of the theory of solids.* Cambridge University Press, Cambridge, UK, second edition, 1979.